Diagnosing ocean feedbacks to the BSISO: SST-modulated surface fluxes and the moist static energy budget

JGR Atmospheres

RESEARCH ARTICLE
10.1029/2018JD029303

Diagnosing Ocean Feedbacks to the BSISO: SST-Modulated Surface Fluxes and the Moist Static Energy Budget

Yingxia Gao[1,2], Nicholas P. Klingaman[2], Charlotte A. DeMott[3], and Pang-Chi Hsu[1]

[1]International Laboratory on Climate and Environment Change and Key Laboratory of Meteorological Disaster of Ministry of Education, Nanjing University of Information Science and Technology, Nanjing, China, [2]National Centre for Atmospheric Science-Climate and Department of Meteorology, University of Reading, Reading, UK, [3]Department of Atmospheric Science, Colorado State University, Fort Collins, CO, USA

Key Points:
- LH is mainly determined by wind-driven flux, while SH is more sensitive to thermodynamic flux
- SST variability increases thermodynamic flux over active BSISO regions, but this is largely offset by wind-driven flux
- SST variability supports convection over the western Indian Ocean, Arabian Sea, and Bay of Bengal, and contributes BSISO propagation

Correspondence to:
Y. Gao,
yingxia@nuist.edu.cn

Citation:
Gao, Y., Klingaman, N. P., DeMott, C. A., & Hsu, P.-C. (2019). Diagnosing ocean feedbacks to the BSISO: SST-modulated surface fluxes and the moist static energy budget. *Journal of Geophysical Research: Atmospheres*, *124*, 146–170. https://doi.org/10.1029/2018JD029303

Received 6 JUL 2018
Accepted 1 DEC 2018
Accepted article online 7 DEC 2018
Published online 11 JAN 2019

Abstract The oceanic feedback to the atmospheric boreal summer intraseasonal oscillation (BSISO) is examined by diagnosing the sea surface temperature (SST) modification of surface fluxes and moist static energy on intraseasonal scales. SST variability affects intraseasonal surface latent heat (LH) and sensible heat (SH) fluxes, through its influence on air-sea moisture and temperature gradients (Δq and ΔT, respectively). According to bulk formula decomposition, LH is mainly determined by wind-driven flux perturbations, while SH is more sensitive to thermodynamic flux perturbations. SST fluctuations tend to increase the thermodynamic flux perturbations over active BSISO regions, but this is largely offset by the wind-driven flux perturbations. Enhanced surface fluxes induced by intraseasonal SST anomalies are located ahead (north) of the convective center over both the Indian Ocean and the western Pacific, favoring BSISO northward propagation. Analysis of budgets of column-integrated moist static energy ($\langle m \rangle$) and its time rate of change ($\partial\langle m \rangle/\partial t$) shows that SST-modulated surface fluxes can influence the development and propagation of the BSISO, respectively. LH and SH variability induced by intraseasonal SSTs maintain 1–2% of $\langle m \rangle$ day^{-1} over the equatorial western Indian Ocean, Arabian Sea, and Bay of Bengal but damp about 1% of $\langle m \rangle$ day^{-1} over the western North Pacific. The contribution of intraseasonal SST variability to $\partial\langle m \rangle/\partial t$ can reach 12–20% over active BSISO regions. These results suggest that SST variability is conducive, but perhaps not essential, for the propagation of convection during the BSISO life cycle.

1. Introduction

The intraseasonal oscillation (ISO) is one of the dominant modes of variability in the tropics. It has significant seasonality in frequency (Hartmann et al., 1992), intensity (Madden, 1986), and propagation (Wang & Rui, 1990). The ISO during boreal winter, also known as the Madden-Julian Oscillation (MJO), is characterized by planetary-scale convective anomalies, with continuous eastward propagation from the western Indian Ocean to the central and eastern Pacific (Madden & Julian, 1971, 1972). The ISO during boreal summer (BSISO) has a more complex structure than the MJO, due to its intense interaction with the Asian summer monsoon (Krishnamurti & Subrahmanyam, 1982; Yasunari, 1979). It exhibits multiple propagation pathways: east and north in the Indian monsoon region (Gadgil & Srinivasan, 1990; Hartmann & Michelsen, 1989; Murakami & Nakazawa, 1985) and northwest over the western North Pacific (Chen & Murakami, 1988; Lau & Chan, 1986; Murakami, 1980). Northward propagation is the most prominent feature of the BSISO. As the BSISO propagates north from the equator into monsoon areas, its activity substantially affects monsoon rainfall (Webster et al., 1998; Wu & Wang, 2001; Zhou & Chan, 2005), tropical cyclones (Hartmann & Maloney, 2001; Straub & Kiladis, 2003), and the occurrence of extreme events (Hsu et al., 2017; Li et al., 2015; Ren et al., 2013; Sun et al., 2016).

Internal atmospheric dynamics are essential to the initiation, development, and propagation of the BSISO (Bellon & Sobel, 2008; Hsu & Weng, 2001; Kawamura et al., 1996; Lawrence & Webster, 2002; Wang & Rui, 1990; Wang & Xie, 1997). Using an intermediate-complexity model, Wang and Xie (1997) suggested the BSISO may originate from Rossby waves, in which the background sea surface temperature (SST) and moisture distribution led to the emanation of Rossby waves from the equatorial Kelvin-Rossby wave packet. Meridionally asymmetric structures of vorticity and moisture with respect to BSISO convection are found in observations and model simulations, which may play an essential role in its northward propagation (Ajayamohan et al., 2011; Bellon & Sobel, 2008; Jiang et al., 2004; Kawamura et al., 1996). The model

results in Wang and Xie (1996) and Xie and Wang (1996) indicate that the interaction between the strong vertical shear of the summer mean flow and equatorial Rossby waves coupled free-atmospheric baroclinic and barotropic modes, which generated barotropic vorticity north of convection (Lawrence & Webster, 2002). Besides the vertical wind shear mechanism, Jiang et al. (2004) also examined the moisture-convection feedback mechanism using reanalysis and an atmospheric general circulation model (AGCM). They showed that both the anomalous moisture advection induced by the mean meridional wind and the mean moisture advection induced by the anomalous meridional wind could contribute to BSISO northward propagation. Due to mean state differences, the mechanisms for BSISO propagation in the Indian Ocean may differ from those in the western Pacific (Chou & Hsueh, 2010; DeMott et al., 2013). High-frequency variability can also feed back upscale to the development and propagation of the large-scale ISO circulation through atmospheric eddy momentum, heat, and moisture transports (Biello & Majda, 2005; Gao et al., 2018; Maloney, 2009; Wang & Liu, 2011; Zhou & Li, 2010).

Air-sea interaction may also contribute to BSISO northward propagation (Kemball-Cook & Wang, 2001; Krishnamurti et al., 1988; Roxy & Tanimoto, 2012; Waliser & Graham, 1993). Warm (cold) SST anomalies are observed ahead of (behind) the BSISO convective center, associated with increased (decreased) shortwave radiative heating (SW) and reduced (enhanced) evaporation related to the anomalous BSISO convection (Hendon & Glick, 1997; Webster, 1983; Woolnough et al., 2000). While the possibility for the feedback of oceanic anomalies to BSISO convection has been discussed often, only a small handful of studies have hypothesized physical mechanisms for this feedback. SST anomalies and their gradients may induce anomalous boundary layer convergence (Lindzen & Nigam, 1987) and destabilize the atmosphere ahead of convection on intraseasonal scales (Hsu & Li, 2012). The anomalous SST can also affect the atmospheric ISO convection by modifying surface fluxes (DeMott et al., 2016; Wang et al., 2018). DeMott et al. (2016) analyzed the effect of intraseasonal SST variability on the MJO by computing surface flux component terms using daily mean and 61-day running mean SST. In the framework of the moist static energy (MSE) budget, the difference between "full SST" and "smoothed SST" flux projections onto column-integrated MSE ($\langle m \rangle$) and its time rate of change ($\partial\langle m \rangle/\partial t$) reveals the SST effect on the MJO $\langle m \rangle$ budget. Intraseasonal SST variability maintains 1–2% of daily equatorial $\langle m \rangle$ anomalies but damps 1–2% of daily subtropical $\langle m \rangle$ anomalies. The SST effect can offset roughly 10% of the equatorial $\langle m \rangle$ loss induced by the vertical advection of $\langle m \rangle$ (10–20% of $\langle m \rangle$ day^{-1}). SST fluctuations also promote MJO eastward propagation, with a contribution of up to 10% of $\partial\langle m \rangle/\partial t$ across the Warm Pool. Recently, Wang et al. (2018) showed that warm SST anomalies to the north of convection tend to increase surface turbulent fluxes by amplifying the air-sea temperature and moisture gradients over the western North Pacific, which promotes BSISO northward propagation by preconditioning the boundary layer for convection.

The role of air-sea coupling in the northward propagation of BSISO has been revealed by modeling studies (Fu et al., 2003; Fu & Wang, 2004; Klingaman et al., 2008; Lin et al., 2011; Rajendran & Kitoh, 2006; Seo et al., 2007). Kemball-Cook et al. (2002) found that the simulated BSISO was more realistic in a coupled general circulation model than in its counterpart AGCM. Fu et al. (2007) showed that the prediction skill of BSISO-related rainfall over the Asian-western Pacific region was about 17 days in the ECHAM4 AGCM, while it extended to about 24 days when the AGCM was coupled to an intermediate-complexity ocean model. Compared to daily coupling frequency, coupled general circulation models with subdaily coupling frequency show improved fidelity for the BSISO (Hu et al., 2015; Klingaman et al., 2008; Woolnough et al., 2007). In contrast, Neena et al. (2017) showed that the skill for BSISO eastward and northward propagation in an AGCM can be as good as, or even better than, that simulated by the coupled version of the same model. This disagreement among modeling studies indicates the role of air-sea interaction in the BSISO has not been fully understood, especially the oceanic feedback to the atmosphere. We address this gap by assessing the effect of SST fluctuations on the BSISO in reanalysis data, which is an important tool for improving our understanding of the climate system.

The importance of MSE in MJO initiation (Peters & Neelin, 2006; Raymond, 2000; Sobel et al., 2014) and propagation (Andersen & Kuang, 2012; Kemball-Cook & Weare, 2001; Maloney, 2009) has been addressed by interrogating reanalyses and numerical experiments. A buildup of MSE occurs before MJO deep convection, and it is discharged during and after the MJO convective and stratiform stages: the so-called recharge-

discharge mechanism for MJO dynamics (Andersen & Kuang, 2012; Bladé & Hartmann, 1993; Johnson et al., 1999; Kiladis et al., 2005). Despite the growing wealth of studies on the MSE budget of the MJO, only a few studies have examined the BSISO MSE budget (e.g., Ajayamohan et al., 2011). This paper investigates oceanic feedbacks to the atmospheric BSISO convection in the context of the MSE budget using two modern reanalyses. We extend the air-sea interaction analysis framework of DeMott et al. (2016) from the boreal winter (November–April) MJO to the boreal summer (May–October) ISO. We further extend DeMott et al. (2016) by considering interbasin differences in the strength of the SST feedback to the BSISO between the Indian and Pacific Oceans, which is critical given the complex structure of the BSISO as it propagates north and east. The paper is organized as follows. The data and diagnostic methods are described in section 2. Section 3 shows the modification of surface flux variability by intraseasonal SSTs. Quantitative contributions of MSE budget terms and SST-rectified surface fluxes to $\langle m \rangle$ and $\partial\langle m \rangle/\partial t$ are shown in section 4. Discussion and summary are given in section 5.

2. Data and Methods

2.1. Data

We diagnose the oceanic feedback to atmospheric BSISO convection by using two reanalyses: the European Centre for Medium-Range Weather Forecasts (ECMWF) Interim Re-Analysis (ERAI) at a resolution of 1.5° × 1.5° (Dee et al. 2011), and the National Aeronautics and Space Administration (NASA) Modern-Era Retrospective Analysis for Research and Applications v2 (MERRA) at a resolution of 1° × 1° (Rienecker et al., 2011). The daily-mean variables from each data set include the following: precipitation, 850-hPa wind speed, longwave radiative heating (LW), SW, surface variables associated with latent heat (LH) and sensible heat (SH) fluxes, and the three-dimensional variables related to MSE and the MSE budget. As the SST boundary condition for ERAI has been prescribed from satellite analyses corrected by buoy observation since 1986 (Reynolds et al., 2002), we use data from 1986 to 2016.

2.2. Surface Flux Decomposition

SST fluctuations exert an impact on the atmosphere, and thus on BSISO activity, through variations in surface fluxes. The surface bulk formulae are adopted to calculate the SST contribution to the intraseasonal LH and SH. LH and SH can be computed as follows (Weare et al., 1981):

$$LH = \rho L_v C_e \Delta q |V|; \Delta q = q^*_{SST} - q_{\text{air}} \tag{1}$$

$$SH = \rho C_p C_h \Delta T |V|; \Delta T = SST - T_{\text{air}} \tag{2}$$

where ρ is near-surface air density; L_v denotes the latent heat of condensation; C_e and C_h are the constant transfer coefficients for moisture and heat, respectively; C_p is the heat capacity of dry air; Δq and ΔT are the specific humidity and temperature differences between the sea surface and the near-surface atmosphere (2 m above the surface), respectively; and $|V|$ is the wind speed at 10 m above the surface. To estimate the relative importance of wind and moisture (heat) fluctuations to LH (SH) variability, the intraseasonal anomalies of LH (SH) are decomposed into three parts:

$$LH^* = \rho L_v C_e \left[\overline{\Delta q} |V|' + \Delta q' \overline{|V|} + \left(\Delta q' |V|' \right)' \right] \tag{3}$$

$$SH^* = \rho C_p C_h \left[\overline{\Delta T} |V|' + \Delta T' \overline{|V|} + \left(\Delta T' |V|' \right)' \right] \tag{4}$$

where the overbar represents the low-frequency (>100 days) background and a prime represents the intraseasonal (20- to 100-day filtered) variability. To distinguish our computed fluxes from the values in the reanalyses themselves (e.g., LH and SH), we write our fluxes as LH^* and SH^*, respectively. In (3) and (4), LH^* and SH^* are decomposed into three terms: the wind-driven ($\overline{\Delta q}|V|'$ and $\overline{\Delta T}|V|'$), thermodynamic ($\Delta q' \overline{|V|}$ and $\Delta T' \overline{|V|}$), and second-order ($(\Delta q' |V|')'$ and $(\Delta T' |V|')'$) flux perturbations. The scaling coefficient of $\rho L_v C_e$ ($\rho C_p C_h$) is determined by regressing the sum of these three flux perturbations onto the total LH (SH) at each grid point. Next, (3) and (4) are recalculated using the SST field without the intraseasonal component (referred to as "noISO SST") in (1) and (2). The difference between LH^* (SH^*) calculated based on the full

and noISO SST can reveal the role of intraseasonal SST variability in LH^* (SH^*). To avoid confusion, LH^* and SH^* derived from the full SST are denoted LH^*_{SST} and SH^*_{SST}, while values derived from the noISO SST are denoted $LH^*_{SST\_noISO}$ and $SH^*_{SST\_noISO}$. Our definition of intraseasonal SST (20- to 100-day filtered) differs from that by DeMott et al. (2016), in which the authors used the departure from 61-day running mean. The choice of definition makes little difference to our results and no difference to our conclusions. We adopt the 20- to 100-day filtered SST to unify the definition of the intraseasonal scale throughout the study.

2.3. The MSE Budget

As in many studies (Kiranmayi & Maloney, 2011; Maloney, 2009) and shown in section 3, the temporal evolution of MSE is highly consistent with that of rainfall; thus, MSE can also be treated as a proxy for convection. The SST effect on BSISO convection can be diagnosed through MSE budget analysis following Neelin and Held (1987). The column-integrated MSE ($\langle m \rangle$) is defined as

$$\langle m \rangle = \langle C_p T \rangle + \langle gZ \rangle + \langle L_v q \rangle \tag{5}$$

where T is temperature, g is gravitational acceleration, Z is geopotential height, and q is specific humidity. Angled brackets denote a mass-weighted vertical integral from 1,000 to 100 hPa. To understand specific processes responsible for MSE temporal variability, the budget for the time rate of change of MSE ($\partial\langle m \rangle/\partial t$) is adopted, which can be written as

$$\frac{\partial \langle m \rangle}{\partial t} = -\langle V \cdot \nabla m \rangle - \left\langle \omega \cdot \frac{\partial m}{\partial p} \right\rangle + \langle LW \rangle + \langle SW \rangle + LH + SH \tag{6}$$

where V is the horizontal wind vector, ∇ is the horizontal gradient operator, ω is the vertical pressure velocity, and p is pressure. The first two terms on the right-hand side in equation (6) are the horizontal and vertical advection of $\langle m \rangle$. The column-integrated LW and SW (i.e., $\langle LW \rangle$ and $\langle SW \rangle$) are calculated as the differences of net fluxes between the top of the atmosphere and the surface.

Figure 1 shows the seasonal mean $\langle m \rangle$ and 850-hPa wind, and the standard deviations of 20- to 100-day filtered $\langle m \rangle$ and $\partial\langle m \rangle/\partial t$. The pattern of mean $\langle m \rangle$ is similar to that of summer mean SST (Figure 2e), and the maximum mean $\langle m \rangle$ is located over South Asia (80°E–120°E, 10°N–25°N). Influenced by the Asian summer monsoon, the low-level circulation is dominated by strong southwesterlies over the Indian Ocean and southeasterlies over the western Pacific. The distributions of intraseasonal variability of $\langle m \rangle$ and $\partial\langle m \rangle/\partial t$ resemble each other, with maxima off the equator in the Northern Hemisphere.

3. Modification of LH and SH Variability by Intraseasonal SST

As the results from the ERAI and MERRA data sets are highly similar, to save space, we show most of our results for ERAI only.

3.1. Contribution of Intraseasonal SST to LH and SH Variability

First, the seasonal mean and standard deviation (σ) of 20- to 100-day filtered variability of surface flux-related variables during boreal summer (May–October) are illustrated in Figure 2. Mean precipitation (Figure 2a) shows large values over the Warm Pool region, Bay of Bengal, and a narrow band in the Pacific from the equator to 10°N, which is the typical boreal summer intertropical convergence zone pattern. Enhanced intraseasonal rainfall variability appears in the Asian summer monsoon region centered in the Bay of Bengal, South China Sea, and Philippine Sea (Figure 2f). Consistent with 850-hPa wind speed (Figure 1a), summer mean 10-m wind speed is higher over the Indian Ocean than over the western Pacific (Figure 2b). The intraseasonal wind speed ($\sigma(V)$) shows the strongest variability over the South China Sea (Figure 2g). The distributions of mean LH and $\sigma(LH)$ (Figures 2c and 2h) are similar to those of surface wind speed, with larger values off the equator than near the equator. The amplitude of SH (Figure 2d) is about an order of magnitude smaller than that of LH. Unlike LH, high mean SH exists over the equatorial regions and the Southern Hemisphere. The pattern of $\sigma(SH)$ over the Northern Hemisphere (Figure 2i) is generally consistent with that of intraseasonal SST (Figure 2j), with vigorous variability along the coasts where the land-sea distribution is complex. With a focus on the tropical oceans, stronger $\sigma(SST)$ is observed over the shallower mixed layers of the Indian Ocean than over the deeper mixed layers of the western Pacific.

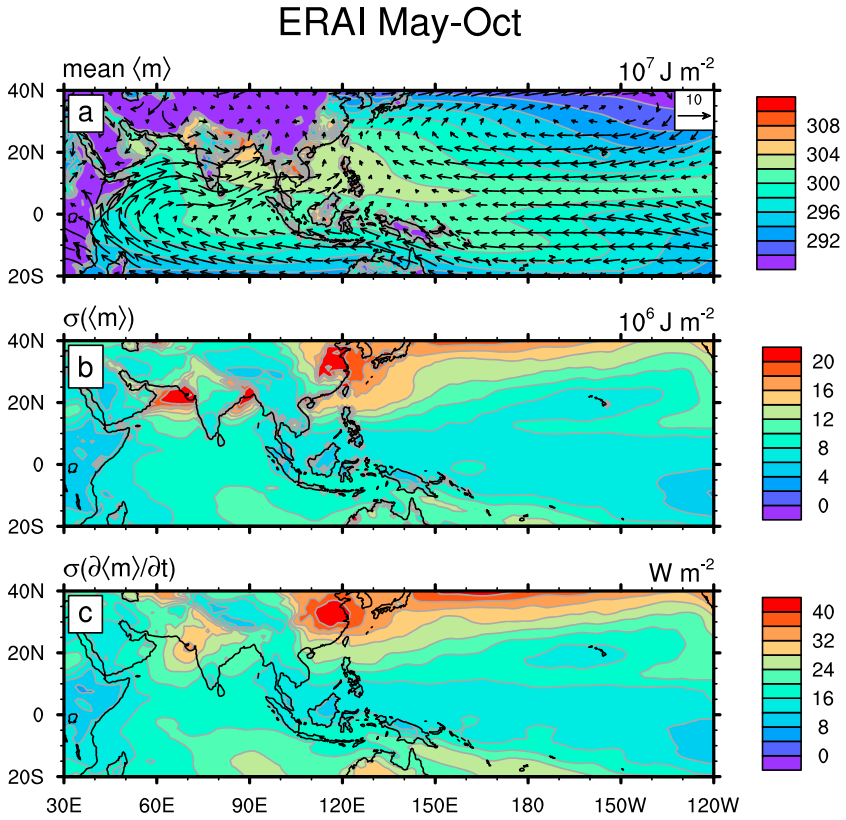

Figure 1. May–October (a) mean $\langle m \rangle$ (shading) and 850-hPa horizontal winds (vectors; m/s), (b) standard deviation of 20- to 100-day filtered $\langle m \rangle$, and (c) standard deviation of 20- to 100-day filtered $\partial \langle m \rangle / \partial t$. ERAI = European Centre for Medium-Range Weather Forecasts (ECMWF) Interim Re-Analysis.

Before diagnosing the SST effect on surface turbulent fluxes (LH and SH), the daily SST skewness during boreal summer is analyzed (Figure 3). Significant positive SST skewness appears over the western Indian Ocean, southern Arabian Sea, and Bay of Bengal, which implies that the amplitude of warm SST anomalies is larger than that of the cold SST anomalies. Negative SST skewness is observed over the South China Sea and Philippine Sea; skewness is weak over the equatorial western Pacific. Strong positive (negative) SST is a consequence of large (small) net surface heat fluxes (Q_{net}) due to enhanced (reduced) SW and calm (strong) winds that decrease (increase) surface turbulent fluxes and ocean vertical mixing. These processes lead to a shoaling (deepening) of the mixed layer depth, which can enhance (weaken) the SST response to the anomalous ISO convection (Duvel et al., 2004; Duvel & Vialard, 2007; Roxy et al., 2013). A stronger oceanic feedback may exist over the western Indian Ocean, Arabian Sea, and Bay of Bengal, as warm SST anomalies may destabilize the atmosphere.

Next, the SST effect on LH and SH is investigated using the bulk formulae calculated from the full and noISO SST (section 2.2). LH^*_{SST} is highly consistent with LH (Figures 4a and 4b), which gives us confidence for further diagnosis. The left-column panels in Figure 4 show the standard deviations of intraseasonally filtered LH, LH^*_{SST}, and its related flux perturbations and components. The wind-driven flux term ($\overline{\Delta q}|V|'$; Figure 4c) is the primary contributor to variations in LH^*_{SST}. There is vigorous $\overline{\Delta q}|V|'$ in the Northern Hemisphere, with maxima in the Arabian Sea, Bay of Bengal, South China Sea, and Philippine Sea. The thermodynamic flux perturbations ($\Delta q'\overline{|V|}$; Figure 4d) show off-equatorial maxima. Minima in $\Delta q'\overline{|V|}$ exist over the equatorial oceans, which are likely due to weak mean wind speed (Figure 2b). The shape of $\Delta q'\overline{|V|}$ over the Northern Hemisphere is largely determined by the air-sea moisture gradient (Figure 4h). The intraseasonal variability of near-surface specific humidity (q_{air}; Figure 4f) is stronger than that of the saturated specific humidity at the SST (q^*_{SST}; Figure 4g), highlighting the importance of q_{air} over q^*_{SST} for LH^*_{SST}. The pattern

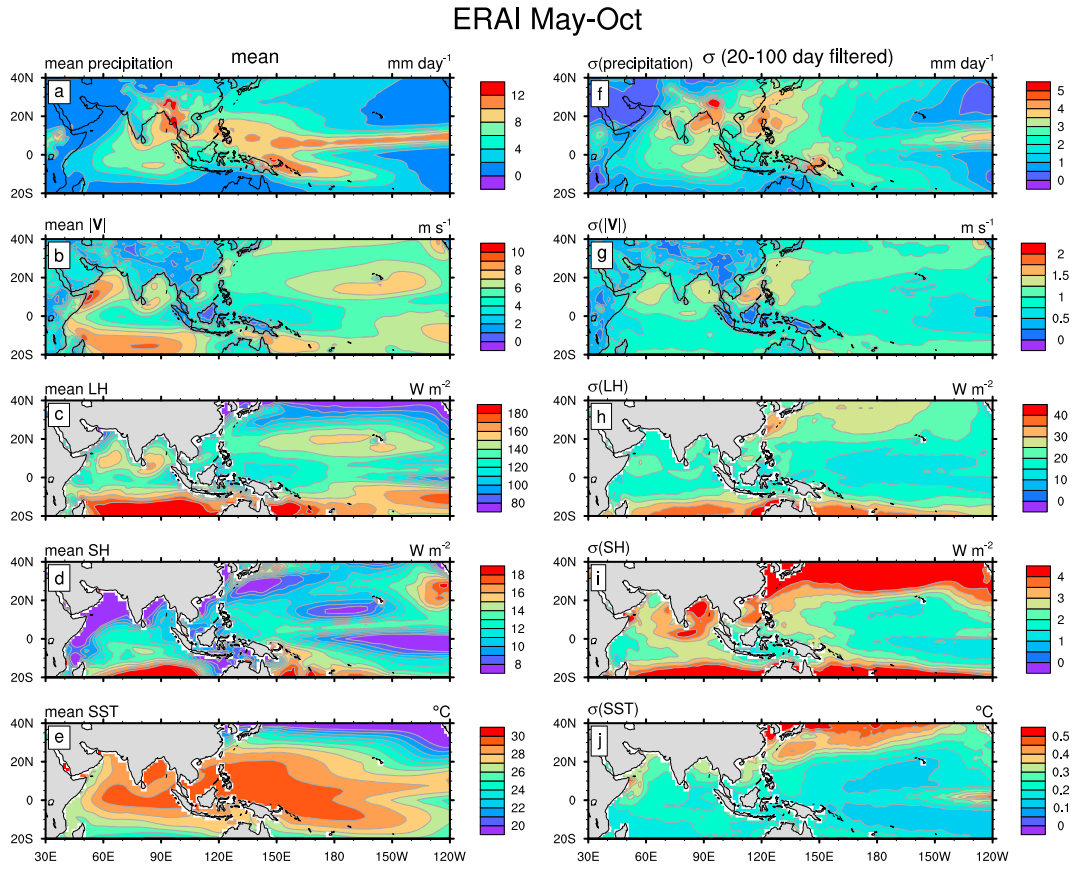

Figure 2. May–October mean of (a) precipitation, (b) 10-m wind speed, (c) LH, (d) SH, and (e) SST. (f–j) The same as (a)–(e), except for the standard deviations of 20- to 100-day filtered time series of each variable. In (c) and (d), upward is positive. LH = latent heat; SH = sensible heat; SST = sea surface temperature; ERAI = European Centre for Medium-Range Weather Forecasts (ECMWF) Interim Re-Analysis.

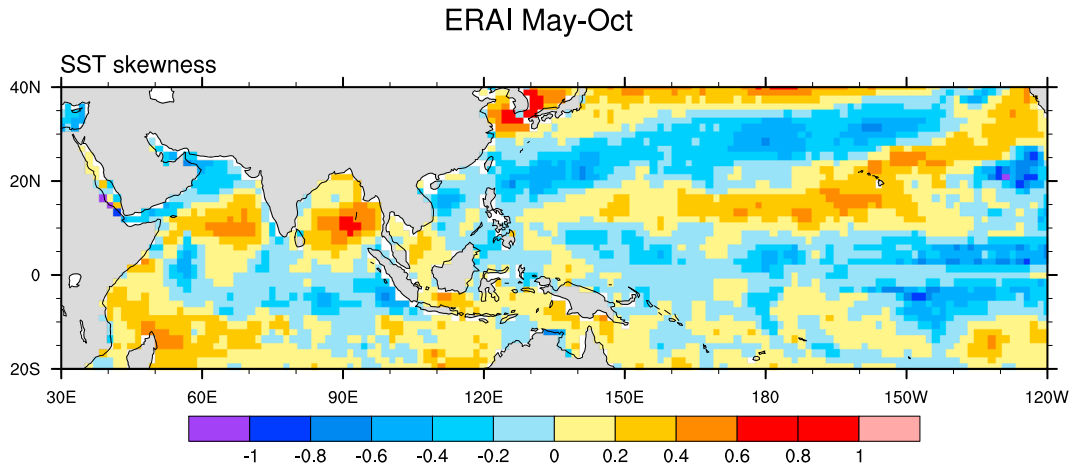

Figure 3. Horizontal distribution of May–October daily SST skewness. SST = sea surface temperature; ERAI = European Centre for Medium-Range Weather Forecasts (ECMWF) Interim Re-Analysis.

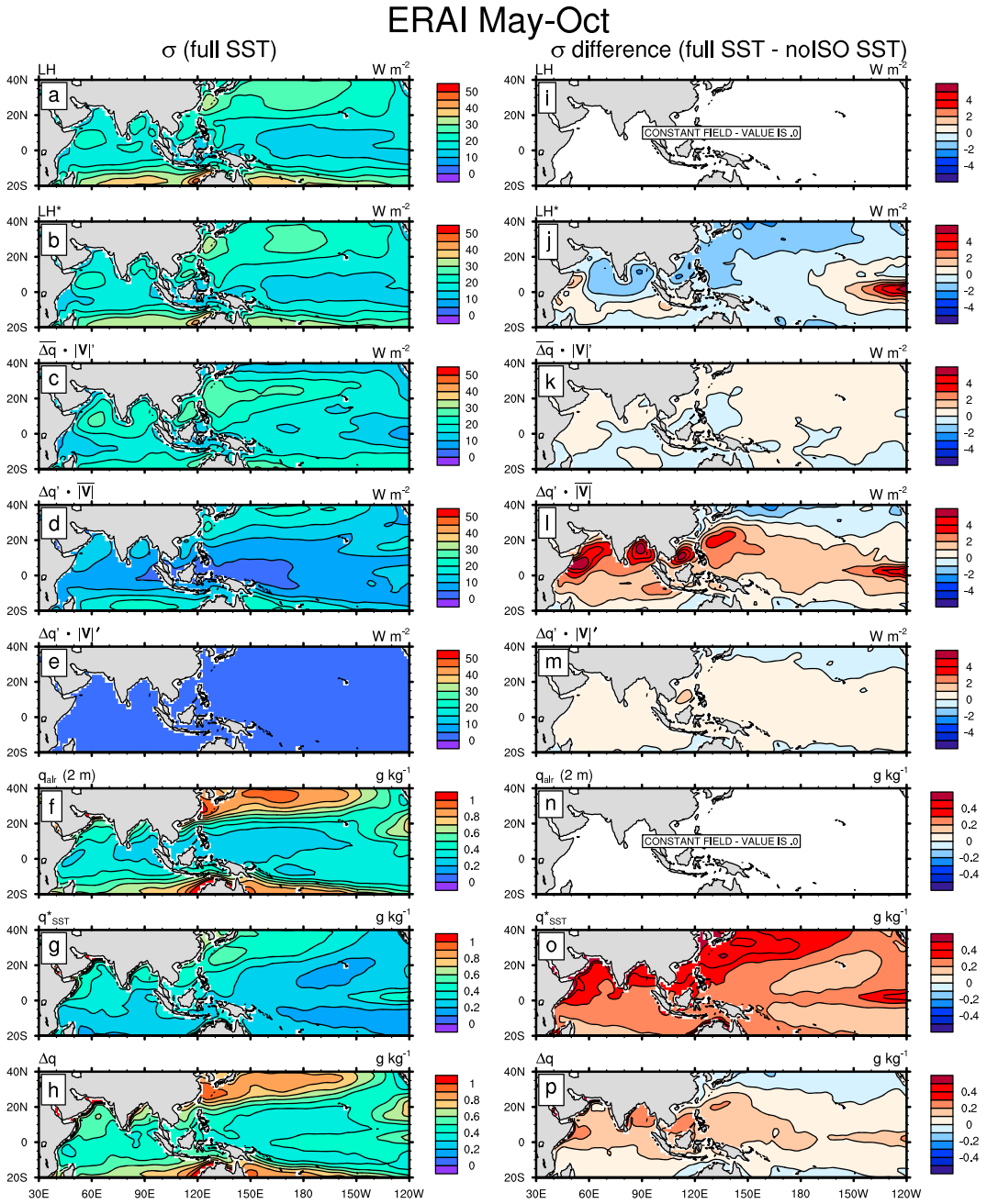

Figure 4. May–October standard deviations of 20- to 100-day filtered (a) LH, (b) LH^*, (c) $\overline{\Delta q}|V|'$, (d) $\Delta q'\overline{|V|}$, (e) $(\Delta q'|V|')'$, (f) q_{air}, (g) q^*_{SST}, and (h) Δq. (i–p) The same as (a)–(h), except the panels show the difference between the values shown in (a)–(h) and the standard deviations of the corresponding variable calculated using SST without the intraseasonal component ("noISO" SST). LH = latent heat; SST = sea surface temperature; ERAI = European Centre for Medium-Range Weather Forecasts (ECMWF) Interim Re-Analysis.

of Δq variability is not simply the spatial difference of Figures 4f and 4g, since q_{air} and q^*_{SST} are out of phase (DeMott et al., 2015; their Figure 17). The combination of q_{air} and q^*_{SST} produces larger $\sigma(\Delta q)$ in the tropical Indian Ocean than in the western Pacific (Hendon & Glick, 1997). The amplitude of the second-order flux perturbations ($(\Delta q'|V|')'$; Figure 4e) is much smaller than those of the other two flux perturbations. To reveal the effect of intraseasonal SST on those variables, Figures 4i–4p show the standard deviation difference of those variables derived from the full and noISO SST. The SST effect on LH^* is substantially negative over most regions of high LH^*_{SST}, which means that intraseasonal SST anomalies decrease LH^*_{SST}

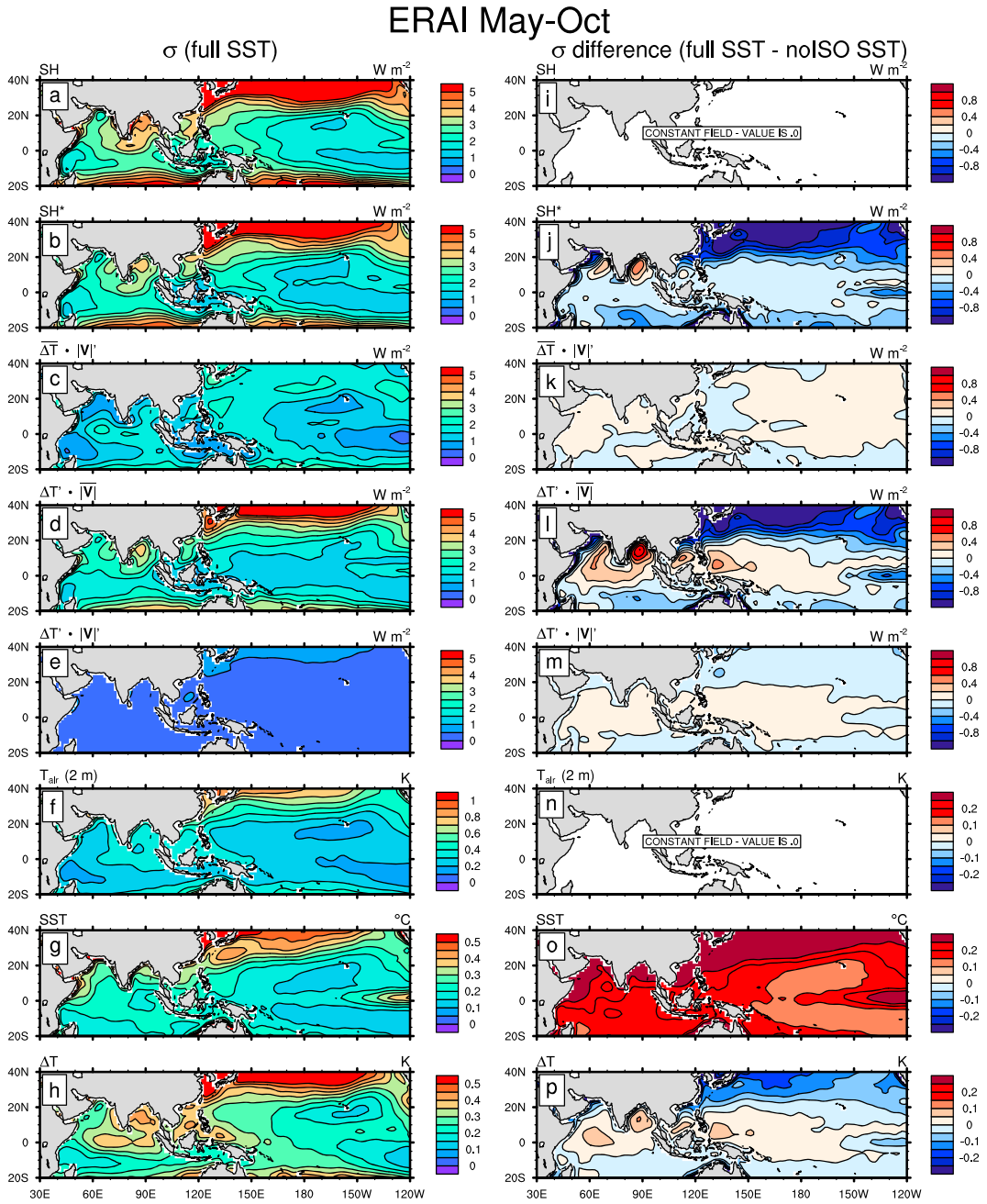

Figure 5. As in Figure 4, except for the variables related to SH.SH = sensible heat; ERAI = European Centre for Medium-Range Weather Forecasts (ECMWF) Interim Re-Analysis.

variability. However, the SST effect on each of the three flux components is positive. This suggests that the component terms offset each other. The reduced LH^* is largely due to the enhanced $\Delta q'\overline{|V|}$, which counteracts $\overline{\Delta q}|V|'$. The $\Delta q'\overline{|V|}$ with full SST is broadly 1–4 W/m^2 larger than $\Delta q'\overline{|V|}$ with noISO SST, and exceeds 4 W/m^2 over the active BSISO regions.

The same approach is applied to SH (Figure 5). As for LH, $\sigma\left(SH^*_{SST}\right)$ highly resembles $\sigma(SH)$. The pattern of $\sigma\left(SH^*_{SST}\right)$ is mainly determined by ΔT (Figures 5b and 5h). This is consistent with the result of DeMott et al. (2014), which suggests the importance of the local ΔT for tropical SH. Over the Indian Ocean, the wind-driven flux perturbation ($\overline{\Delta T}|V|'$) is smaller than the thermodynamic flux perturbation ($\Delta T'\overline{|V|}$), while $\Delta T'$

$\overline{|V|}$ is smaller than $\overline{\Delta T}|V|'$ over the equatorial western Pacific (Figures 5c and 5d). $\Delta T'\overline{|V|}$ increases with latitude, controlled by ΔT. The SST effect on SH^* component terms is shown in Figures 5i–5p. The intraseasonal SST exerts significant influence on SH^* north to 10°N. Enhanced SH^* derived from SST variability is seen over a small region in the Arabian Sea and Bay of Bengal, while SST-modulated component flux terms (Figures 5k–5m) display increased variability over much broader regions. Thus, the component terms of SH^*_{SST} also offset one another but less so than the components of LH^*_{SST}. The positive effect of SST variability on $\Delta T'\overline{|V|}$ occurs within 20°N of the equator, with a contribution of about 0.2–0.6 W/m^2. In summary, the intraseasonal SST can substantially increase the thermodynamic flux perturbations ($\Delta q'\overline{|V|}$ and $\Delta T'\overline{|V|}$) over the Asian summer monsoon region, indicating a potentially nonnegligible role of SST fluctuations for BSISO convection.

3.2. Role of SST Fluctuations in BSISO Northward Propagation

In this section, the SST effect on BSISO northward propagation is investigated through lead-lag composites. The composites of variables are constructed with respect to two reference domains that represent the two major regions of BSISO activity: the eastern Indian Ocean (75°E–85°E, 0°–10°N) and the western Pacific (140°E–150°E, 0°–10°N).

Figure 6 shows the lag regression coefficients of $\langle m\rangle$ and its tendency terms onto the intraseasonal precipitation during the BSISO life cycle (lag ±25 days) over the Indian Ocean. The 20- to 100-day filtered (75°E–85°E) averaged variables are regressed onto the 20- to 100-day filtered (75°E–85°E, 0°–10°N) averaged rainfall, as a function of latitude, to reveal the northward propagating features associated with the BSISO. Note that in DeMott et al. (2016), unfiltered variables are regressed onto filtered rainfall. We examined both methods and found that the choice makes little qualitative difference to the results, which implies that intraseasonal component of the unfiltered variable has the strongest linear relationship to the filtered rainfall, relative to other components of the unfiltered variable. The convection displays an apparent northward propagation, with a speed of about 1.8 m/s. At lag 0, intraseasonal convection reaches its maximum. The structure of $\langle m\rangle$ is highly in phase with the intraseasonal rainfall, with enhanced (reduced) $\langle m\rangle$ within the active (suppressed) BSISO region (Figure 6a). Intense moistening occurs approximately 1 week prior to the convection maximum (Figure 6f). Following Andersen & Kuang, (2012), we assume that components that are in phase with $\langle m\rangle$ affect the convection maintenance, while processes that are in phase with $\partial\langle m\rangle/\partial t$ are related to the propagation of BSISO convection. Figures 6b–6e and 6g–6j show the results for MSE tendency terms on the right-hand side of equation (6). We note that the sum of these terms is smaller than $\partial\langle m\rangle/\partial t$, with about 30–40% underestimation. This suggests the MSE budget is not closed in these reanalyses; some processes are missing or miscalculated. Further, the propagation speed of the sum of terms is somewhat slower than that of $\partial\langle m\rangle/\partial t$, with maxima slightly shifting toward the strongest convection. These residuals are related to the deficiencies of precipitation in the atmospheric models on which the reanalyses depend (Adames & Wallace, 2015; Mapes & Bacmeister, 2012). Despite these residuals, the MSE budget equation provides a useful tool to evaluate the contribution of each process to $\partial\langle m\rangle/\partial t$. $\langle m\rangle$ is dissipated by the vertical and horizontal advection of $\langle m\rangle$ ($-\langle\omega\cdot\partial m/\partial p\rangle$ and $-\langle|V|\cdot\nabla m\rangle$; Figures 6b–c), as they exhibit positive (negative) values over suppressed (active) convection. However, $-\langle\omega\cdot\partial m/\partial p\rangle$ and $-\langle|V|\cdot\nabla m\rangle$ maximize over the suppressed convection center and ahead (north) of the active convection center, respectively. Thus, $\partial\langle m\rangle/\partial t$ is largely supported by $-\langle|V|\cdot\nabla m\rangle$, particularly by the zonal advection of $\langle m\rangle$ ($-\langle u\cdot\partial m/\partial x\rangle$). The meridional advection of $\langle m\rangle$ ($-\langle v\cdot\partial m/\partial y\rangle$) only increases $\partial\langle m\rangle/\partial t$ for equatorial convection (Figures 6c–6e). Column-integrated LW ($\langle LW\rangle$) is the primary contributor to $\langle m\rangle$ (Figure 6g), with a secondary contribution from LH (Figure 6h), although the maximum LH lags the convective center slightly. SH and $\langle SW\rangle$ also support $\langle m\rangle$ but with weaker amplitude (Figures 6i and 6j).

Intraseasonal SST can feed back to BSISO convection by modifying LH and SH. Figure 7 shows the SST effects on LH^* (left panels) and SH^* (right panels) over the eastern Indian Ocean. The second-order term is small and neglected here. As expected, the wind-driven flux perturbation of LH^*_{SST} ($\overline{\Delta q}|V|'$, red) is much larger than the thermodynamic term of LH^*_{SST} ($\Delta q'\overline{|V|}$, solid blue). $\Delta q'\overline{|V|}$ leads $\overline{\Delta q}|V|'$ by about 2 weeks, such that they are nearly out of phase. Thus, the amplitude of LH^*_{SST} (solid magenta) is smaller than that of $\overline{\Delta q}|V|'$.

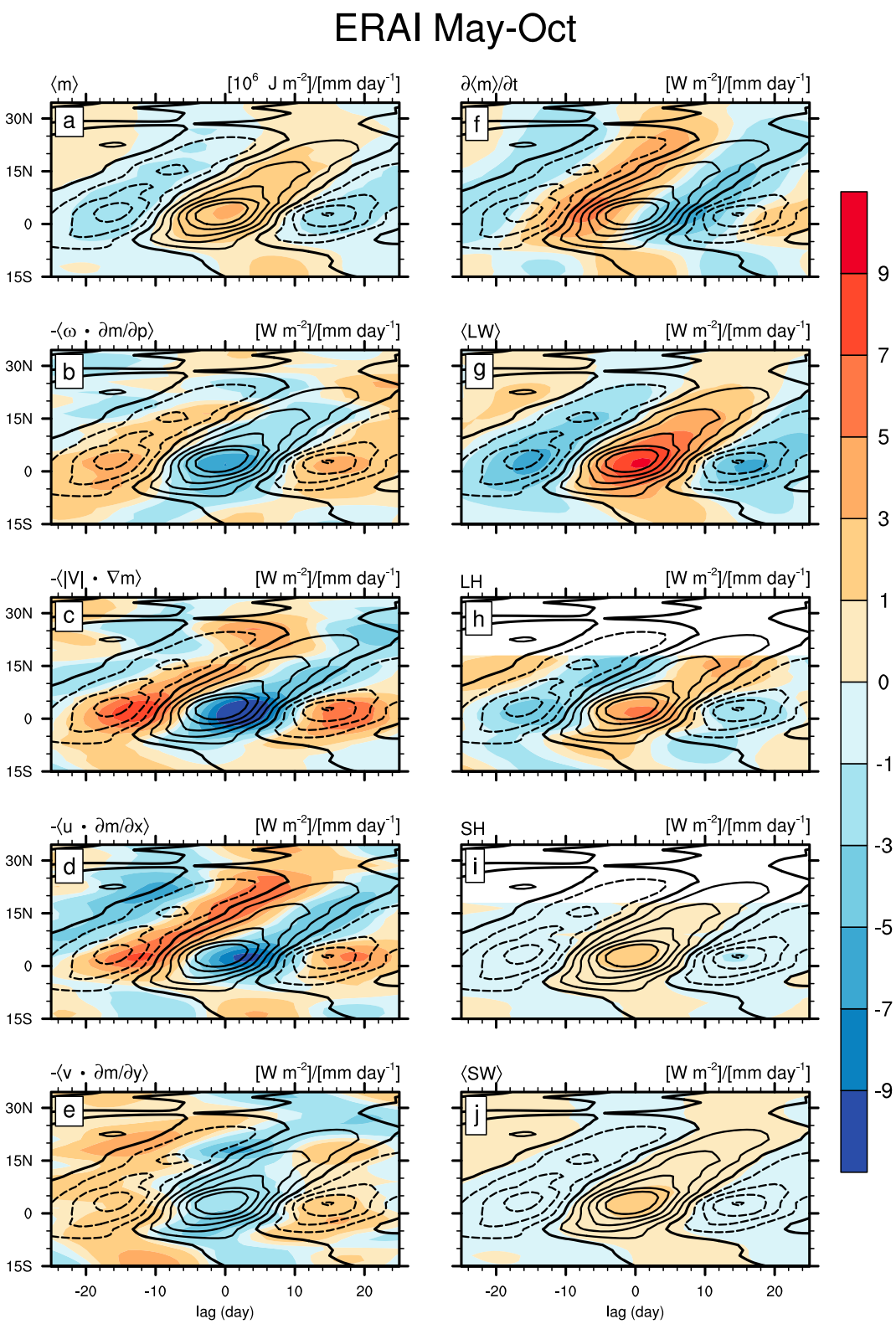

Figure 6. Lagged regression coefficients of 20- to 100-day filtered (75°E–85°E) averaged moist static energy budget terms onto 20- to 100-day filtered (75°E–85°E, 0°–10°N) averaged rainfall as a function of latitude: (a) $\langle m \rangle$, (b) $-\langle \omega \cdot \partial m/\partial p \rangle$, (c) $-\langle |V| \cdot \nabla m \rangle$, (d) $-\langle u \cdot \partial m/\partial x \rangle$, (e) $-\langle v \cdot \partial m/\partial y \rangle$, (f) $\partial \langle m \rangle/\partial t$, (g) $\langle LW \rangle$, (h) LH, (i) SH, and (j) $\langle SW \rangle$. Regression coefficients of rainfall are overlaid with an interval of 0.2 (mm/day)/(mm/day). The white shading in (h) and (i) indicates missing values over land areas. LW = longwave radiative heating; LH = latent heat; SH = sensible heat; SW = shortwave radiative heating; ERAI = European Centre for Medium-Range Weather Forecasts (ECMWF) Interim Re-Analysis.

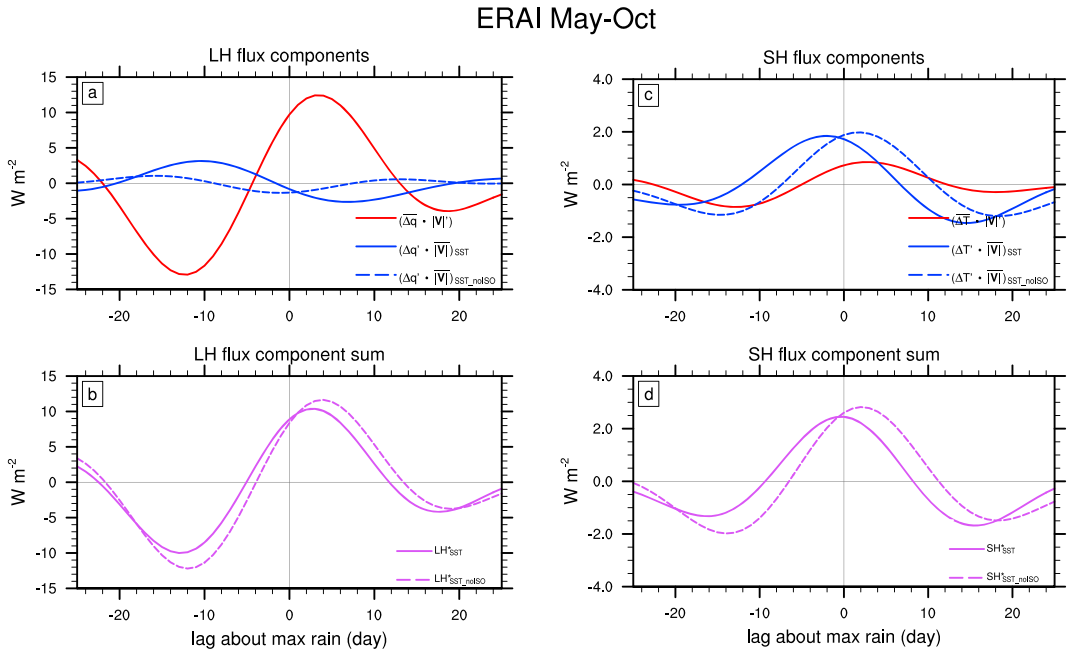

Figure 7. (a) Lagged regression coefficients of (a) $\overline{\Delta q}|V|'$ (red), $\Delta q'|\overline{V}|_{SST}$ (solid blue), $\Delta q'|\overline{V}|_{SST\_noISO}$ (dashed blue), and (b) LH^*_{SST} (solid magenta) and $LH^*_{SST\_noISO}$ (dashed magenta) onto 20- to 100-day filtered rainfall, averaged over the eastern Indian Ocean (75°E–85°E, 0°–10°N). (c–d) The same as (a)–(b), except for the variables associated with SH. LH = latent heat; SH = sensible heat; SST = sea surface temperature; ERAI = European Centre for Medium-Range Weather Forecasts (ECMWF) Interim Re-Analysis.

When the intraseasonal SST is removed, $\Delta q'|\overline{V}|$ is reduced and shifts toward longer leads (dashed blue). As a consequence, compared to the component LH^* using the noISO SST ($LH^*_{SST\_noISO}$, dashed magenta), the maximum LH^* using the full SST (LH^*_{SST}) shifts toward the convective center (+1 day), 1 day earlier than the maximum $LH^*_{SST\_noISO}$ (+2 days). The right panel in Figure 7 shows the SST effect on SH^*. SH^*_{SST} is more sensitive than LH^*_{SST} to SST. $\overline{\Delta T}|V|'$ and $\Delta T'|\overline{V}|$ both maintain convection, with about 2 days' phase difference. Without the intraseasonal SST, there are significant phase changes in $\Delta T'|\overline{V}|$, from 1 day ahead of convection to 1 day behind. Correspondingly, SH^*_{SST} is located at the convective center, while $SH^*_{SST\_noISO}$ lags convection.

We next analyze the role of flux perturbations and intraseasonal SST in the northward propagation of BSISO convection. The phase relationships between the convection and wind-driven, thermodynamic, and second-order flux perturbations over the Indian Ocean are shown in Figures 8a–8c. Positive wind-driven flux perturbations appear at and south of the convective center throughout the BSISO life cycle, which is consistent with Figures 7a and 7c. This indicates that wind-driven flux perturbations support BSISO convection but are not favorable for northward propagation. The enhanced wind-driven flux south of the convective center is due to the stronger wind speeds from the BSISO-related southwesterly anomalies superimposed on the background southwesterly monsoon flow. In contrast, the thermodynamic flux perturbations (Figure 8b) maximize ~10 days before the strongest convection. They reduce the degree to which the wind-driven flux perturbations slow BSISO propagation. Off the equator, it is slightly shifted toward the convective center, supporting the convection. Second-order flux perturbations (Figure 8c) are smaller than the other two perturbations; their spatial structure resembles noise. The sum of these three terms is the component total flux (Figure 8d), which is highly similar to the wind-driven flux term (Figure 8a). The difference between the surface component total fluxes calculated from the full and noISO SST (Figures 8d–8f) reveals the role of intraseasonal SST in the surface fluxes associated with the BSISO. It is obvious that the surface fluxes from intraseasonal SSTs maximize about 10 days before convection. The "SST effect" on surface fluxes is approximately 1 W/m^2, which

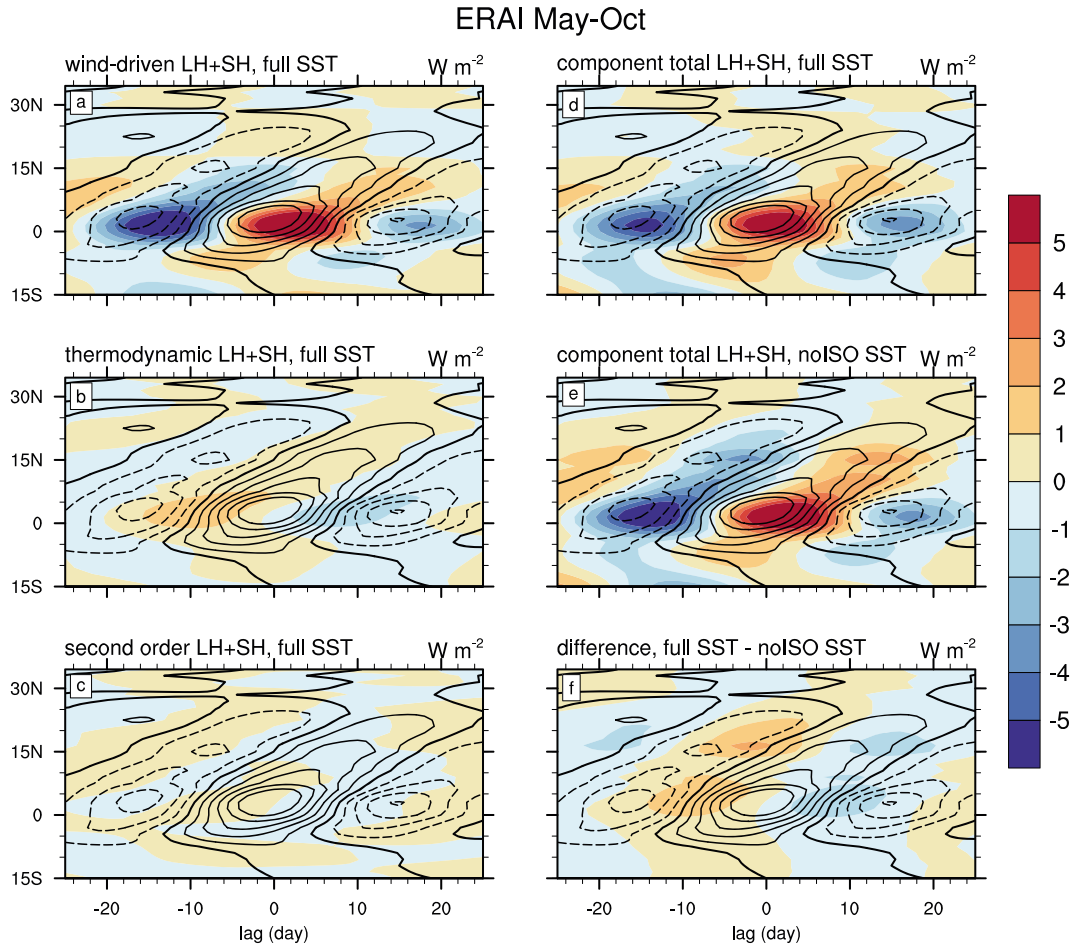

Figure 8. As in Figure 6, except for (a) $\overline{\Delta q}|V|' + \overline{\Delta T}|V|'$ (wind-driven flux perturbations), (b) $\Delta q'\overline{|V|} + \Delta T'\overline{|V|}$ (thermodynamic flux perturbations), (c) $(\Delta q'|V|') + (\Delta T'|V|')$ (second-order flux perturbations), (d) $LH^*_{SST} + SH^*_{SST}$ (the sum of (a)–(c), which are calculated based on the full SST), (e) $LH^*_{SST\_noISO} + SH^*_{SST\_noISO}$ (the component total flux calculated based on the "noISO" SST), and (f) the difference between (d) and (e). LH = latent heat; SH = sensible heat; SST = sea surface temperature; ERAI = European Centre for Medium-Range Weather Forecasts (ECMWF) Interim Re-Analysis.

represents about 20–25% of the total fluxes. Off the equator, the positive anomalies are larger than the negative anomalies. This may be associated with the substantial positive SST skewness over the Bay of Bengal (Figure 3). The SST effect promotes more evaporation and boundary layer heating north of convection, which is conductive to BSISO northward propagation over the Indian Ocean.

The phase relationships between the convection and surface flux perturbations over the western Pacific are shown in Figure 9. The 140°E–150°E averaged variables are regressed onto the (140°E–150°E, 0°–10°N) averaged intraseasonal rainfall. The convection over the western Pacific also exhibits significant northward propagation, with a faster speed than over the Indian Ocean. For equatorial convection, the maximum wind-driven flux perturbation lags ~4 days behind the strongest convection. As the convection moves northward, the flux anomaly shifts toward the convective center and even slightly leads convection (Figure 9a). The thermodynamic flux perturbation (Figure 9b) is positive ahead of convection over the equatorial western Pacific. Off the equator, it is out of phase with convection. The structure of the second-order term (Figure 9c) resembles that of the thermodynamic flux perturbation: It leads convection within 15°N of the equator. It is interesting that the SST effect on surface fluxes over the western Pacific is still positive at negative lags and negative at positive lags, promoting northward propagation. However, in more detail, a positive SST effect appears across the suppressed convection region, while the SST effect over the Indian Ocean is nearly in quadrature with the convection. The

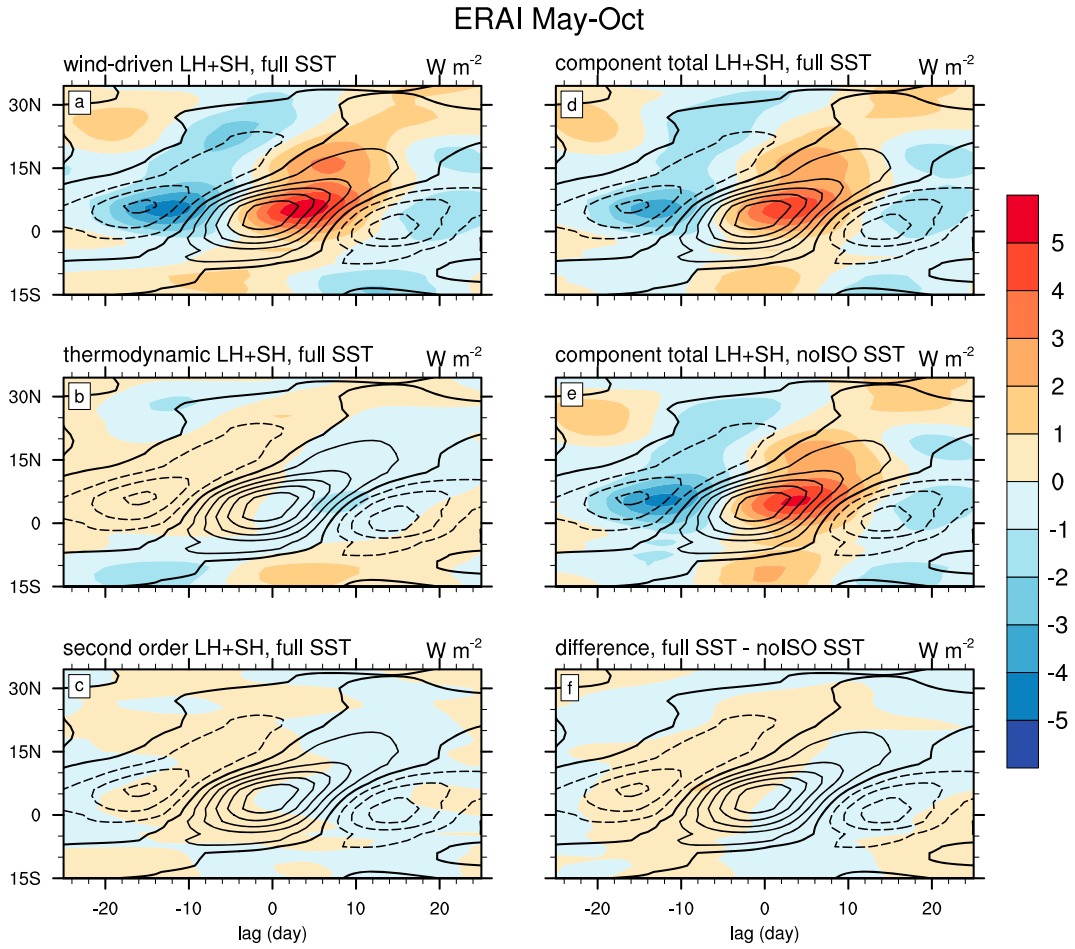

Figure 9. As in Figure 8, except for the 140°E–150°E averaged variables regressed onto 20- to 100-day filtered (140°E–150°E, 0°–10°N) averaged rainfall.

SST effect on convection over the western Pacific may differ from that over the Indian Ocean, despite it contributing to northward propagation in both basins. Besides, the SST effect is weaker in the western Pacific than in the Indian Ocean (Figures 8f and 9f), which might be a consequence of weak SST skewness over the equatorial western Pacific and strong negative SST skewness over the off-equatorial western Pacific (Figure 3), or because of the different phasing between q_{air} and q^*_{SST} in the two basins (Hendon & Glick, 1997). As a whole, intraseasonal SST favors the northward propagation of convection over both the Indian Ocean and western Pacific. Besides BSISO northward propagation, we also analyzed the SST effect on the eastward and westward propagating BSISO modes in the Indian Ocean and western Pacific, respectively. Results for the SST effect on zonal propagation in the Indian Ocean are largely similar to those in DeMott et al. (2016) for the boreal winter MJO. In the western Pacific, the SST effect on zonal propagation is similar to that in the Indian Ocean, except that in the western Pacific the BSISO propagation is mostly westward rather than eastward and has a faster phase speed. Maximum surface fluxes induced by intraseasonal SST significantly leads convection as well, suggesting that SST fluctuations are important for BSISO propagation (figures not shown).

Next, we examine why the role of the wind-driven flux perturbation varies during different stages in the BSISO life cycle over the western Pacific, while it always slows the convection over the Indian Ocean. Figure 10 illustrates the regression coefficients of $\langle m \rangle$ (shading) and 850-hPa winds (vectors) at various lags onto intraseasonal rainfall (contours) in the Indian Ocean and west Pacific. The temporal and spatial distribution of $\langle m \rangle$ moves coherently with rainfall throughout the BSISO life cycle. Equatorial

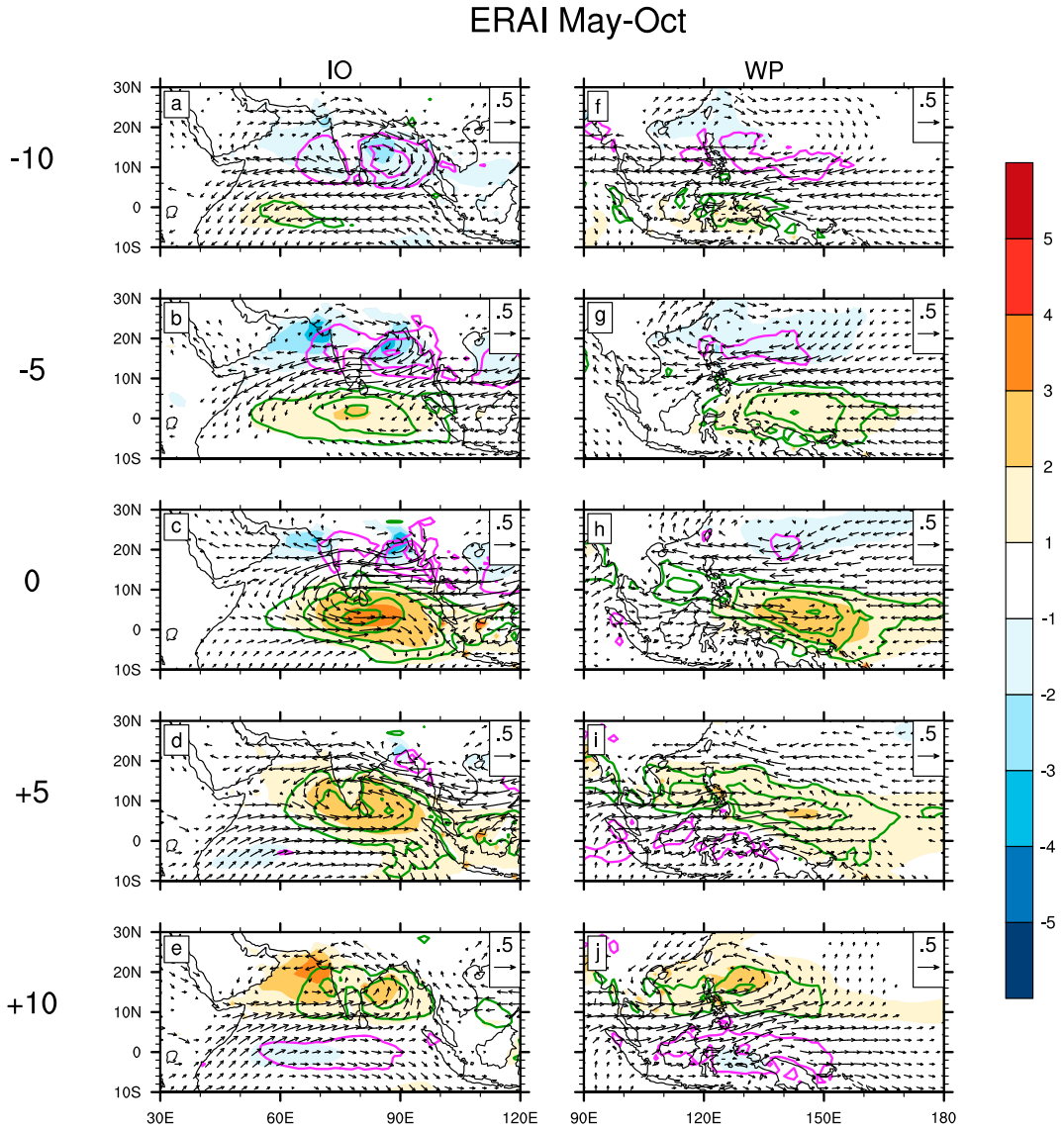

Figure 10. Regression coefficients of 20- to 100-day filtered ⟨m⟩ (shading; (10^6 J/m^2)/(mm/day)), rainfall (contours; (mm day)/(mm/day)), and 850-hPa wind speed (vectors; (m/s)/(mm/day)) at lags of (a) −10, (b) −5, (c) 0, (d) +5, and (e) +10 days, onto 20- to 100-day filtered (75°E–85°E, 0°–10°N) averaged rainfall over the Indian Ocean (IO). (f–j) The same as (a)–(e), except for the variables regressed onto 20- to 100-day filtered (140°E–150°E, 0°–10°N) averaged rainfall over the western Pacific (WP). Regression coefficients of rainfall are overlaid with an interval of 0.3 (mm/day)/(mm/day); positive (negative) values are represented by green (magenta) contours. ERAI = European Centre for Medium-Range Weather Forecasts (ECMWF) Interim Re-Analysis.

convection induces a southerly anomaly to its south and a northeasterly anomaly to its north (Figures 10b, 10c, 10g, and 10h). Thus, there are stronger winds south of convection over both the Indian Ocean and the western Pacific, from the combination of southerly wind anomalies with the mean state winds (southwesterly over the Indian Ocean and southeasterly over the western Pacific; Figure 1a). When the convection moves off the equator, an anomalous cyclone appears northwest of the convection (Figures 10d, 10e, 10i, and 10j) as part of the Rossby wave response to BSISO heating (Gill, 1980) and/or the interaction between the anomalous vertical motion and background vertical shear (Jiang et al., 2004). This anomalous cyclone produces larger wind-driven flux perturbations to the south (north) of convection over the eastern Indian Ocean (western Pacific), when coupled with the background southwesterly (southeasterly).

4. Quantitative Contributions of MSE Budget Terms and SST Variability to BSISO

In this section, we aim to calculate the quantitative contributions of each moistening process (P), including SST variability, to the maintenance and propagation of BSISO convection by regressing each process onto intraseasonal $\langle m\rangle$ and $\partial\langle m\rangle/\partial t$ ($R(\langle m\rangle, P)$, $R(\partial\langle m\rangle/\partial t, P)$). Following DeMott et al. (2016), the fractional contribution of a given process to $\langle m\rangle$, $F_{\langle m\rangle}(P)$, is derived by converting $R(\langle m\rangle, P)$ to units of % $\langle m\rangle$ day^{-1}. Similarly, the fractional contribution of a given process to $\partial\langle m\rangle/\partial t$, $F_{\partial\langle m\rangle/\partial t}(P)$, is derived by converting $R(\partial\langle m\rangle/\partial t, P)$ to units of % $\partial\langle m\rangle/\partial t$:

$$F_{\langle m\rangle}(P) = R(\langle m\rangle, P)*100*86,400 \text{ s day}^{-1} \tag{7}$$

$$F_{\partial\langle m\rangle/\partial t}(P) = R(\partial\langle m\rangle/\partial t, P)*100 \tag{8}$$

The geographic distributions of $F_{\langle m\rangle}(P)$ and $F_{\partial\langle m\rangle/\partial t}(P)$ illustrate the contribution of a given process to the maintenance/damping and generation/destruction of $\langle m\rangle$ (i.e., the development and propagation of convection). Figure 11 shows the fractional contributions of the MSE budget terms to the intraseasonal $\langle m\rangle$ (Figures 11a–11h) and $\partial\langle m\rangle/\partial t$ (Figures 11i–11p). Obviously, $<LW>$ is the most important contributor to intraseasonal $\langle m\rangle$ (Figure 11a). It supports the convection symmetrically about the equator, maximizing on the equator. The distribution of $F_{\langle m\rangle}(LH)$ (Figure 11f) is similar to that of intraseasonal precipitation (Figure 2f) and maintains convection over the active BSISO regions. Maintenance of $\langle m\rangle$ also comes from SH over the tropical regions and $<SW>$ over all areas (Figures 11g and 11h). $\langle m\rangle$ is destroyed by $-\langle\omega\cdot\partial m/\partial p\rangle$ over the entire Warm Pool and by $-\langle|V|\cdot\nabla m\rangle$ over the tropical oceans (Figures 11b and 11c). In contrast, the advection of $\langle m\rangle$ contributes most to $\partial\langle m\rangle/\partial t$, particularly $-\langle|V|\cdot\nabla m\rangle$, which contributes more than 70% of $\partial\langle m\rangle/\partial t$. The distribution of $F_{\partial\langle m\rangle/\partial t}(LH)$ (Figure 11n) is negative over the equatorial and northern Indian Ocean and positive over the northern Philippine Sea. This is consistent with Figures 8d and 9d, as LH^*_{SST} always lags BSISO convection in the Indian Ocean, while LH^*_{SST} transitions from lagging convection to leading convection when the BSISO moves north over the western Pacific. It is interesting that SH contributes not only to the maintenance but also to the generation of $\langle m\rangle$ over most active BSISO regions (Figures 11g and 11o), although the contributions are not as large as those for LH. SH may be important in the development and propagation of BSISO convection.

Over the ocean, the horizontal advection of $\langle m\rangle$ ($-\langle|V|\cdot\nabla m\rangle$) dominates $\partial\langle m\rangle/\partial t$. $F_{\partial\langle m\rangle/\partial t}(-\langle|V|\cdot\nabla m\rangle)$ is larger over the Indian Ocean (80%) than over the western Pacific (>60%), which may be related to the position of Asian summer monsoon trough over the western Pacific. $-\langle|V|\cdot\nabla m\rangle$ is mainly controlled by the zonal advection of $\langle m\rangle$ ($-\langle u\cdot\partial m/\partial x\rangle$). This differs from the study of Jiang et al. (2004), which only emphasized the importance of meridional moisture advection for the northward propagation (Chou & Hsueh, 2010; DeMott et al., 2013). It may be attributed to the background southerly flow in the eastern Indian Ocean, where northward propagation is most obvious. Our results verify that the meridional advection of $\langle m\rangle$ dominates the horizonal advection of $\langle m\rangle$ over the Bay of Bengal (Figure 11). The zonal advection of $\langle m\rangle$ also contributes to the propagation, but with weaker amplitude. $F_{\partial\langle m\rangle/\partial t}(-\langle u\cdot\partial m/\partial x\rangle)$ is larger than $F_{\partial\langle m\rangle/\partial t}(-\langle v\cdot\partial m/\partial y\rangle)$ over the equatorial Indian Ocean and western Pacific. However, $-\langle v\cdot\partial m/\partial y\rangle$ is more important to $\partial\langle m\rangle/\partial t$ over the Bay of Bengal, South China Sea, and coastal East Asia. Particularly, over the South China Sea, $-\langle v\cdot\partial m/\partial y\rangle$ contributes most to $\partial\langle m\rangle/\partial t$, while $-\langle u\cdot\partial m/\partial x\rangle$ tends to decrease $\partial\langle m\rangle/\partial t$. We further decompose $-\langle u\cdot\partial m/\partial x\rangle$ and $-\langle v\cdot\partial m/\partial y\rangle$ to show that over the Indian Ocean, the advection of mean $\langle m\rangle$ by perturbation zonal wind ($-\langle u'\cdot\partial\overline{m}/\partial x\rangle$) is the largest source for $-\langle u\cdot\partial m/\partial x\rangle$. The strong anomalous easterlies north of the convection import the background zonal gradient of $\langle m\rangle$ to the northeast of BSISO convection, as the maximum climatological $\langle m\rangle$ is located over South Asia (Figures 1 and 10). Over the Bay of Bengal, the advection of anomalous $\langle m\rangle$ by the mean meridional wind ($-\langle\overline{v}\cdot\partial m'/\partial y\rangle$) is the largest of the horizonal $\langle m\rangle$ advection terms. The southerlies become much stronger over the Bay of Bengal (Figure 1a), which transport the enhanced $\langle m\rangle$ near the convective center to the north (Figure 10). $-\langle\overline{v}\cdot\partial m'/\partial y\rangle$ also enhances northward propagation over the South China Sea and western Pacific, as revealed by Wang et al. (2018), in which they reported the importance of the anomalous moisture by mean meridional wind ($-\langle\overline{v}\cdot\partial q'/\partial y\rangle$) to the northward propagation of convection. The anomalous $\langle m\rangle$ advection by the anomalous zonal wind ($-u'\cdot\partial m'/\partial x$) is negative over the South China Sea, largely inhibiting propagation.

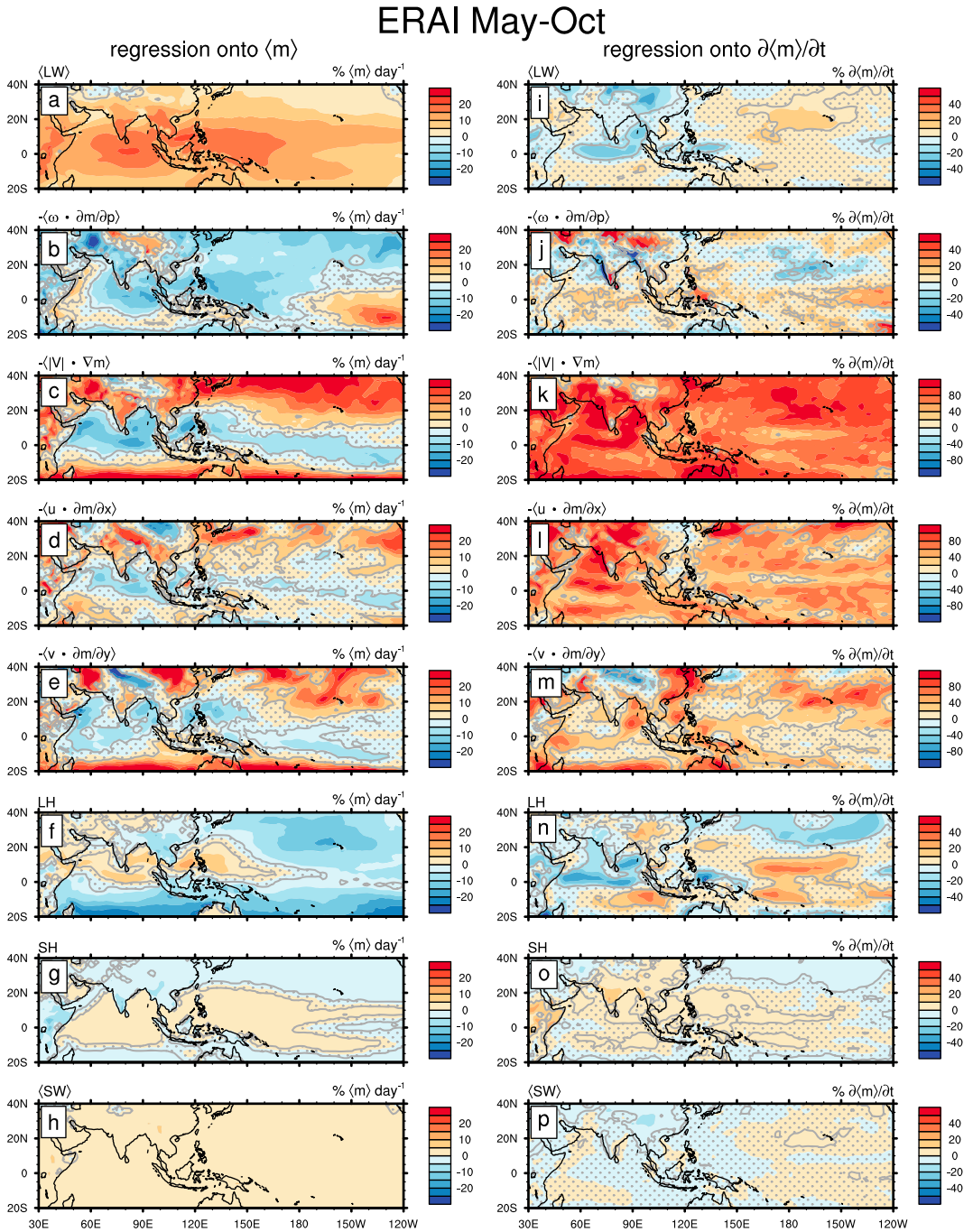

Figure 11. Regression coefficients of 20- to 100-day filtered moist static energy budget terms onto 20- to 100-day filtered $\langle m \rangle$: (a) $\langle LW \rangle$, (b) $-\langle \omega \cdot \partial m/\partial p \rangle$, (c) $-\langle |V| \cdot \nabla m \rangle$, (d) $-\langle u \cdot \partial m/\partial x \rangle$, (e) $-\langle v \cdot \partial m/\partial y \rangle$, (f) LH, (g) SH, and (h) $\langle SW \rangle$. (i–p) The same as (a)–(h), except for the variables regressed onto $\partial \langle m \rangle/\partial t$. The stippled areas are not statistically significant at the 5% level. LW = longwave radiative heating; LH = latent heat; SH = sensible heat; SW = shortwave radiative heating; ERAI = European Centre for Medium-Range Weather Forecasts (ECMWF) Interim Re-Analysis.

The fractional contributions of flux perturbations associated with LH to $\langle m \rangle$ are shown in Figures 12a–12e. The high similarity between $F_{\langle m \rangle}(LH)$ and $F_{\langle m \rangle}\left(LH^*_{SST}\right)$ again verifies that LH is well represented by LH^*_{SST}. Unlike LH and LH^*_{SST}, $\overline{\Delta q}|V|'$ can support convection not only over the active BSISO regions but also over the southern Indian Ocean and the equatorial and eastern Pacific (Figures 12a–12c). In contrast, $\Delta q'\overline{|V|}$ damps

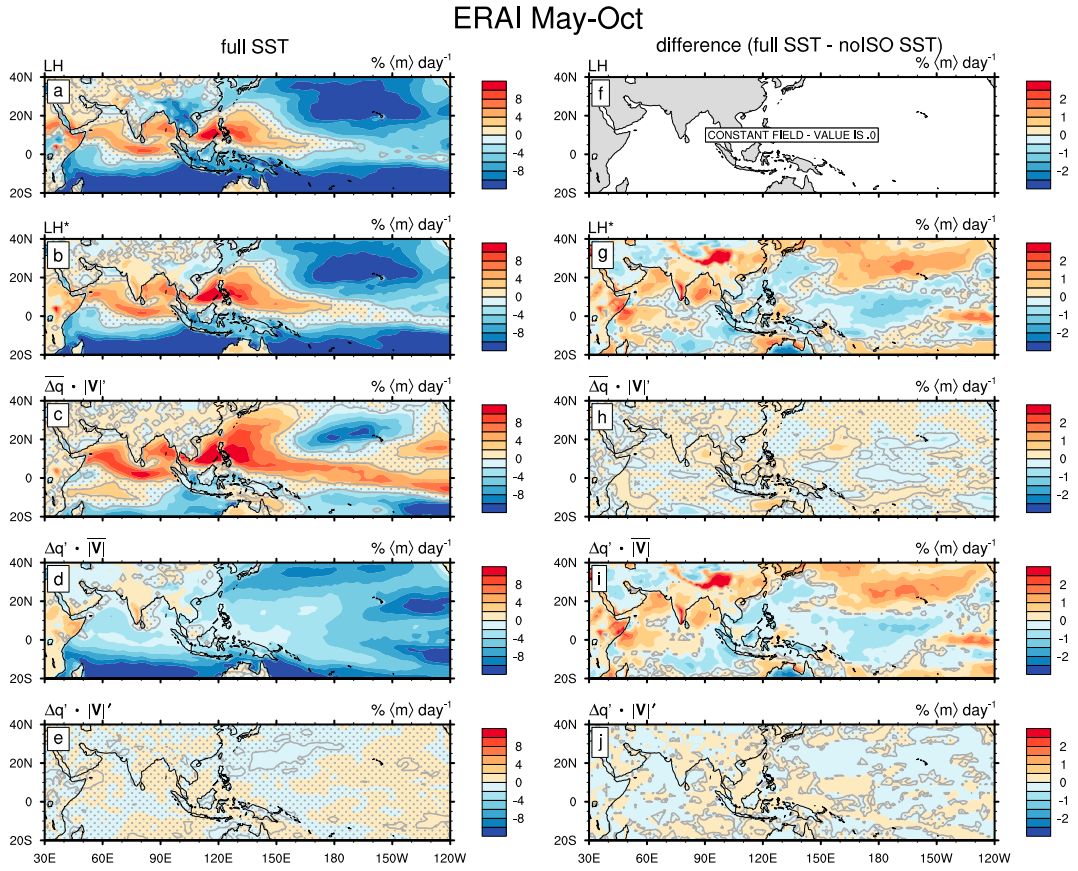

Figure 12. Same as Figures 11a–11e, except for (a) LH, (b) LH^*, (c) $\overline{\Delta q}|V|'$, (d) $\Delta q'\overline{|V|}$, and (e) $(\Delta q'|V|')$. (f–j) The differences between (a)–(e) and the regressed coefficients of the corresponding variable calculated based on the "noISO" SST. LH = latent heat; SST = sea surface temperature; ERAI = European Centre for Medium-Range Weather Forecasts (ECMWF) Interim Re-Analysis.

intraseasonal variability over all ocean areas (Figure 12d), especially over cold SSTs in the Southern Hemisphere and central and eastern Pacific (Figure 2e). The combination of these two leading terms results in positive LH^*_{SST} over the active BSISO regions. The difference between $F_{\langle m\rangle}\left(LH^*_{SST}\right)$ and $F_{\langle m\rangle}\left(LH^*_{SST\_noISO}\right)$ illustrates the intraseasonal SST effect on $\langle m\rangle$ (Figure 12g). Positive values, mainly contributed by the SST effect on $\Delta q'\overline{|V|}$, are observed over the far western Indian Ocean, Arabian Sea, and Bay of Bengal. Over the far western Indian Ocean, SST variability strengthens $\langle m\rangle$ anomalies during the BSISO initiation, contributing about 1.5% of $\langle m\rangle$ day^{-1}. We also examined the contributions of flux perturbations to $\partial\langle m\rangle/\partial t$ (figure not shown). Wind-driven flux perturbations inhibit propagation over the Asian summer monsoon regions, except for a small region over the Philippine Sea, as the perturbations always lag the convection (Figures 8 and 9). Thermodynamic flux perturbations contribute to propagation across the active BSISO region.

Figure 13 shows the total effect of intraseasonal SST variability on $\langle m\rangle$ and $\partial\langle m\rangle/\partial t$ through modifying LH^* and SH^*, using ERAI and MERRA. They are obtained by subtracting $F_{\langle m\rangle}\left(LH^*_{SST\_noISO}+SH^*_{SST\_noISO}\right)$ from $F_{\langle m\rangle}\left(LH^*_{SST}+SH^*_{SST}\right)$ and $F_{\partial\langle m\rangle/\partial t}\left(LH^*_{SST\_noISO}+SH^*_{SST\_noISO}\right)$ from $F_{\partial\langle m\rangle/\partial t}\left(LH^*_{SST}+SH^*_{SST}\right)$. The strong resemblance between these two reanalyses suggests that the intraseasonal SST effects on $\langle m\rangle$ and $\partial\langle m\rangle/\partial t$ are robust. The SST-modulated LH^* accounts for more than 12% of $\partial\langle m\rangle/\partial t$. The contribution of SST variability to $F_{\langle m\rangle}(SH^*)$ and $F_{\partial\langle m\rangle/\partial t}(SH^*)$ (Figures 13b, 13e, 13h, and 13k) is about 20–25% of those for $F_{\langle m\rangle}(LH^*)$ and $F_{\partial\langle m\rangle/\partial t}(LH^*)$ (Figures 13a, 13d, 13g, and 13j), with very similar geographic distributions. They result in a stronger SST effect on $\langle m\rangle$ and $\partial\langle m\rangle/\partial t$. The SST contributions to $F_{\langle m\rangle}(LH^*+SH^*)$ show large values over the equatorial western and central Indian Ocean, northern Arabian Sea, and Bay of Bengal, with contributions

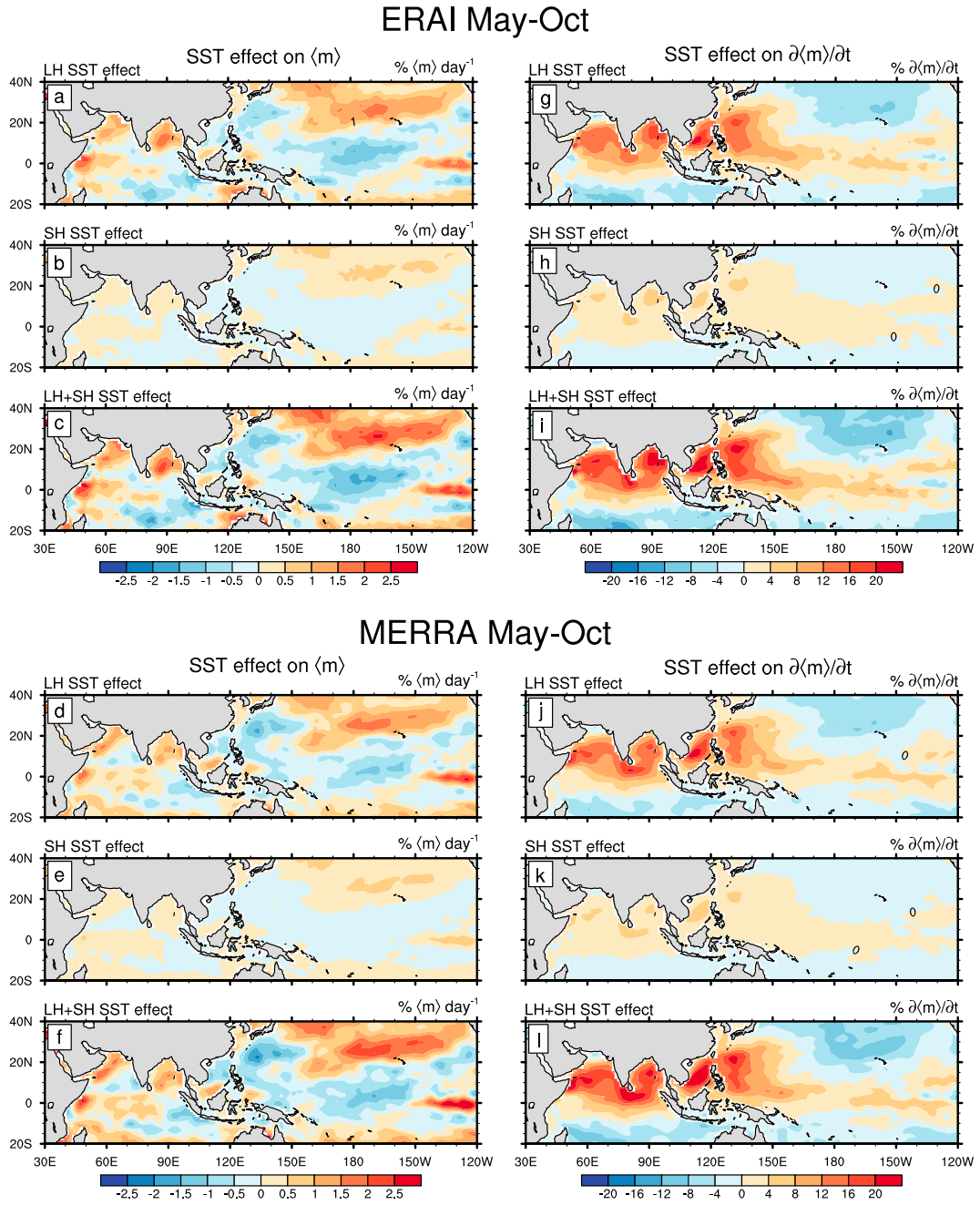

Figure 13. (top) The SST effect on (a–c) $\langle m \rangle$ and (g–i) $\partial\langle m \rangle/\partial t$ via the modifications of (a, g) LH^*, (b, h) SH^*, and (c, i) $LH^* + SH^*$ derived from the ERAI data. (bottom) (d–f and j–l) The same as (a)–(c) and (g)–(i), except using the MERRA data. SST = sea surface temperature; LH = latent heat; SH = sensible heat; ERAI = European Centre for Medium-Range Weather Forecasts (ECMWF) Interim Re-Analysis; MERRA = Modern-Era Retrospective Analysis for Research and Applications v2.

1–2% of $\langle m \rangle$ day^{-1}. Negative SST effects on $\langle m \rangle$ appear over the South China Sea and western North Pacific. Intraseasonal SST contributes to up to 20% of $\partial\langle m \rangle/\partial t$ over the entire active BSISO region, favoring propagation.

It is interesting that the SST effects on $\langle m \rangle$ and $\partial\langle m \rangle/\partial t$ are positive over most of the Indian Ocean but negative on $\langle m \rangle$ and positive on $\partial\langle m \rangle/\partial t$ over the western Pacific. To further understand this, Figures 14 and 15 show lagged regressions of the intraseasonal SST and SST-modulated flux anomalies (LH^* and SH^*) onto the

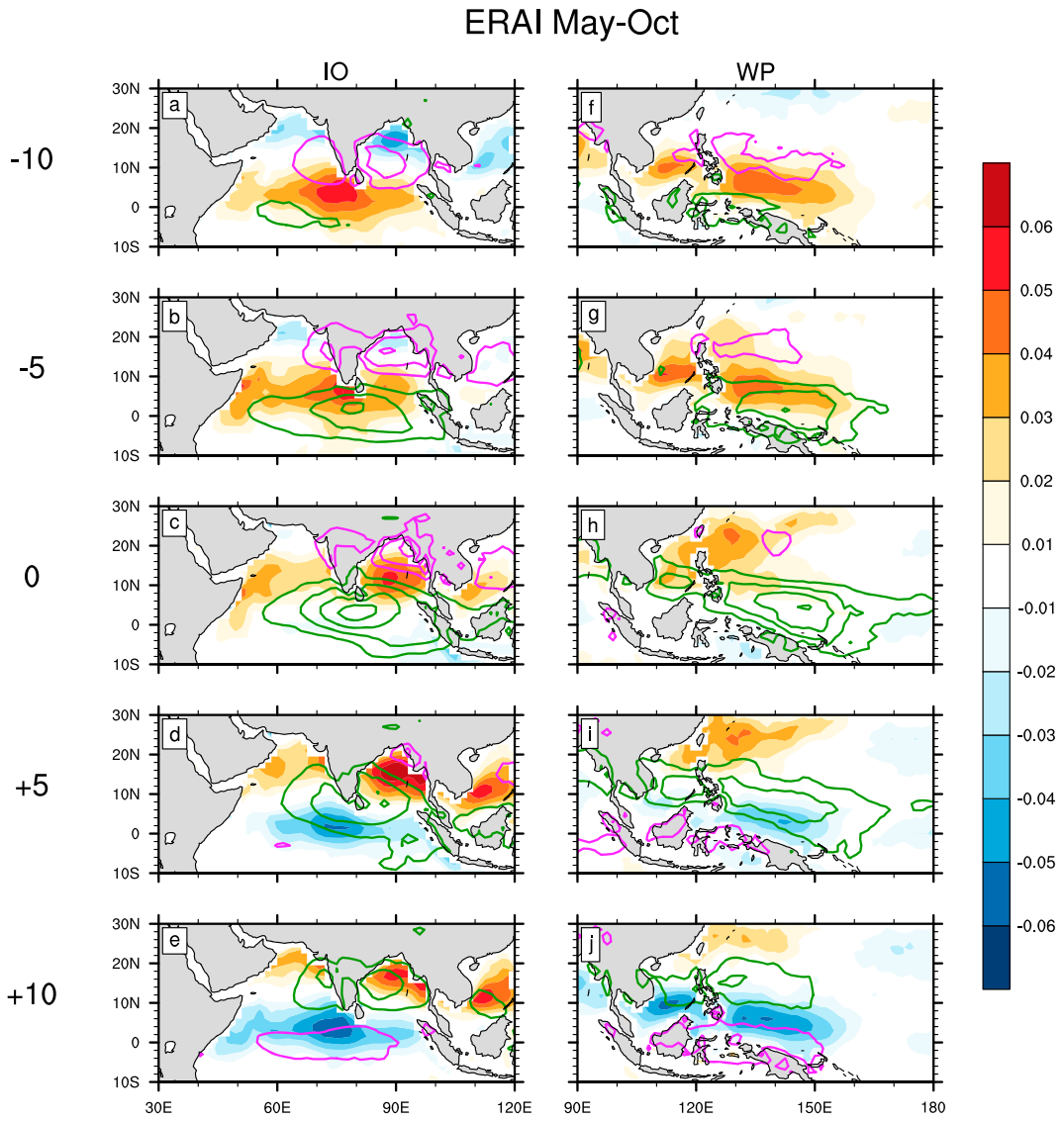

Figure 14. Regression coefficients of 20- to 100-day filtered SST (shading; (K)/(mm/day)) at lags of (a) −10, (b) −5, (c) 0, (d) +5, and (e) +10 days, onto 20- to 100-day filtered (75°E–85°E, 0°–10°N) averaged rainfall over the Indian Ocean (IO). (f–j) The same as (a)–(e), except for the variables regressed onto 20- to 100-day filtered (140°E–150°E, 0°–10°N) averaged rainfall over the western Pacific (WP). Regression coefficients of rainfall are overlaid with an interval of 0.3 (mm/day)/(mm/day); positive (negative) values are represented by green (magenta) contours. ERAI = European Centre for Medium-Range Weather Forecasts (ECMWF) Interim Re-Analysis.

intraseasonal rainfall over the Indian Ocean and western Pacific, respectively. Obviously, SST-modulated flux anomalies (shading in Figure 15) are coherent with the SST anomalies (shading in Figure 14) over the Indian Ocean (left panels) and western Pacific (right panels). Over the Indian Ocean, warm SST and enhanced fluxes always appear to the northeast of the convective center, conductive to propagation from the equatorial west/central Indian Ocean to the Bay of Bengal. Positive intraseasonal SST and flux anomalies lead the convection. Particularly, when convective anomalies are over the equatorial central Indian Ocean and Bay of Bengal at −5 and +10 days (Figures 14b and 14e and Figures 15b and 15e), respectively, warm SST and enhanced fluxes appear over the convective center. This suggests the intraseasonal SST can support convection over the equatorial central Indian Ocean and Bay of Bengal, where the SST effect on $\langle m \rangle$ shows large positive values (Figures 13c and 13f). Over the western Pacific, at negative lags (−10 and −5 days; Figures 14f and 14g and Figures 15f and 15g), positive SST and flux

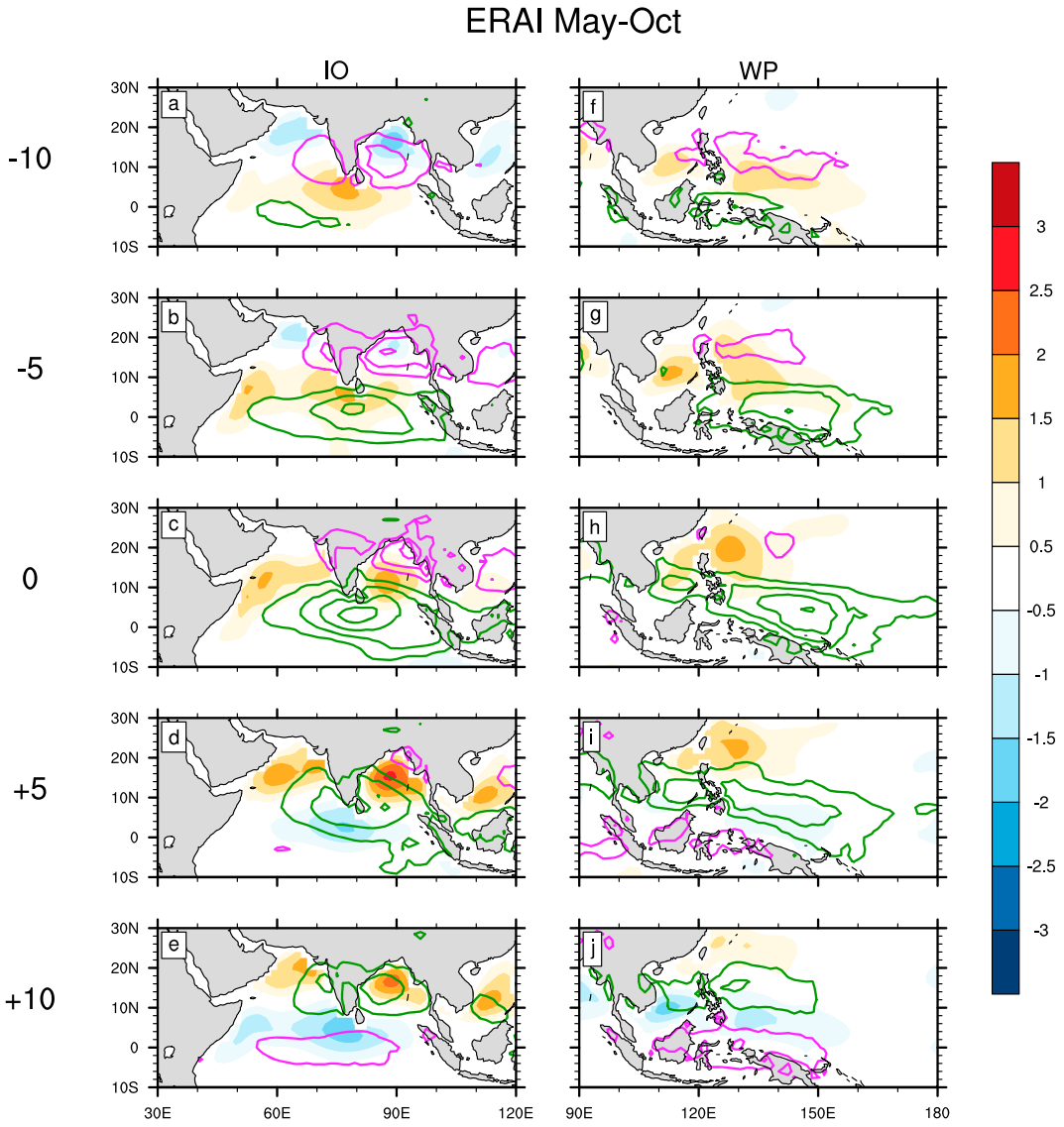

Figure 15. As in Figure 14, except for SST-modulated surface flux anomalies ($LH^* + SH^*$) ((W/m^2)/(mm/day)). SST = sea surface temperature; LH = latent heat; SH = sensible heat.

anomalies show near-quadrature phase relationships with convection. However, as the convection further develops and moves off the equator, descending motion (suppressed convection) ahead of the active convection becomes very weak or even absent (Figures 14h–14j and 15h–15j). At lag +0, the intraseasonal SST is out of phase with convection (Figures 14h and 15h). At +5 and +10 days, positive SST and SST-induced flux anomalies lead 180° ahead of the convection (Figures 14i–14j and 15i–15j). There are weak and negative SST and flux anomalies over the convective region. Thus, the intraseasonal SST tends to damp the BSISO convection over the western Pacific, particularly over the off-equatorial regions where the SST effect on $\langle m \rangle$ is negative (Figures 13c and 13f).

5. Discussion and Summary

5.1. Discussion

This study extends the diagnostic framework of DeMott et al. (2016) to the BSISO; it is useful to compare our results for the BSISO with those from DeMott et al. (2016) for the MJO. In their study, similarly,

maximum LH slightly lags MJO convection; thus, it can maintain $\langle m \rangle$ but cannot contribute to $\partial\langle m \rangle/\partial t$. In winter, SH supports convection over the active MJO region but only contributes to $\partial\langle m \rangle/\partial t$ over the Indian Ocean, unlike in boreal summer, when it supports convection and contributes to $\partial\langle m \rangle/\partial t$ across the active BSISO region. $\langle m \rangle$ ahead (east) of MJO convection is opposed by $\overline{\Delta q}|V|'$ and supported by $\Delta q'\overline{|V|}$; these two terms strongly offset each other. MJO and BSISO $\langle m \rangle$ is primarily maintained by $\langle LW \rangle$ and reduced by the vertical and horizontal advection of $\langle m \rangle$. The oceanic feedbacks to the MJO and BSISO are remarkably similar over the Indian Ocean. SST anomalies support convection during initiation over the western Indian Ocean. Intraseasonal SST fluctuations ahead of convection favor MJO and BSISO propagation, with contributions larger than 10% and 12% of $\partial\langle m \rangle/\partial t$, respectively. Results for boreal summer ISO are generally consistent with those for boreal winter MJO, which may be due to strong association between BSISO and MJO (Lawrence & Webster, 2002). Unlike DeMott et al. (2016), we find a strong difference in SST feedbacks over the Indian Ocean and western Pacific, associated with differences in the boreal summer background state in these basins. As a result of the interaction between anomalous wind speed and background wind speed, wind-driven flux perturbations and horizonal advection of $\langle m \rangle$ play different roles in BSISO convection in these basins. What is more, while the intraseasonal SST contributes to the convection northward propagation over both basins, it supports $\langle m \rangle$ over the Indian Ocean but damps $\langle m \rangle$ over the western Pacific. This is related to the different phase relationships between convection and intraseasonal SST, as well as between convection and SST-modulated flux anomalies.

Although the SST effects on $\langle m \rangle$ and $\partial\langle m \rangle/\partial t$ from ERAI and MERRA are similar, issues in both products may affect the robustness of our results. The root mean square difference of daily ERAI and MERRA LH (SH) from buoy observations is approximately 20–40 W/m^2 (4–5 W/m^2) over the Asian summer monsoon region, despite ERAI and MERRA assimilating some buoy data (10-m wind, 2-m air temperature, and 2-m relative humidity; Bentamy et al., 2017). Dry biases in near-surface specific humidity are strongly correlated with the positive LH biases (Brunke et al., 2011; Praveen Kumar et al., 2012; Sanchez-Franks et al., 2018). Sanchez-Franks et al. (2018) also show that cold biases in SST, relative to buoy data, appear in both ERAI and MERRA; they attribute these biases to the common use of the Operational Sea Surface Temperature and Sea Ice Analysis (OSTIA) foundation SST product (Donlon et al., 2012). Therefore, our "SST effect" may be slightly underestimated.

Wang et al. (2018) found that the intraseasonal SST anomalies could induce boundary layer moisture convergence and increase surface turbulent flux anomalies, which tend to heat and moisten the boundary layer, favoring the northward propagation of BSISO. Based on our diagnostics, intraseasonal SST variability contributes up to 20% to the propagation of convection ($\partial\langle m \rangle/\partial t$). Although the SST effect enhances propagation, the intraseasonal SST variability alone could not drive propagation; most of the "work" of propagation is accomplished by the atmospheric circulation. The BSISO circulation also exerts a strong control on the pattern of intraseasonal SST (Hendon & Glick, 1997; Woolnough et al., 2000), such that air-sea feedbacks to the BSISO are themselves coupled to the circulation. Thus, the internal atmospheric dynamics are essential to the northward propagation of BSISO convection, with the assistance of oceanic feedbacks.

5.2. Summary

The effect of intraseasonal SST on boreal summer ISO activity is examined through reanalysis diagnostics within an MSE framework. The patterns of intraseasonal column-integrated MSE ($\langle m \rangle$) and its time rate of change ($\partial\langle m \rangle/\partial t$) resemble each other, with maxima off the equator in the Northern Hemisphere. Summer mean $\langle m \rangle$ maximizes over South Asia. Influenced by the Asian summer monsoon, the low-level circulation is dominated by strong southwesterlies over the Indian Ocean and southeasterlies over the western Pacific. The precipitation shows significant intraseasonal variability over the Asian summer monsoon regions. Enhanced intraseasonal SST appears over the Warm Pool region and northern Pacific, with stronger variability in the Indian Ocean than in the western Pacific associated with mixed-layer depth differences. Significant positive SST skewness is observed over the southern Arabian Sea and Bay of Bengal, while negative skewness exists over the Philippine Sea.

Based on bulk formula decomposition, LH and SH are divided into three parts: the wind-driven, thermodynamic, and second-order flux perturbations. While LH is mainly determined by the wind-driven flux perturbations, SH is more sensitive to the thermodynamic flux perturbations. The wind-driven and

thermodynamic flux perturbations associated with LH tend to offset each other, while for SH these two terms support convection. Over the Indian Ocean and equatorial western Pacific, the wind-driven flux perturbation slightly lags convection, while the maximum thermodynamic flux perturbation leads convection. This suggests the thermodynamic perturbation reduces the degree to which the wind-driven perturbation slows BSISO propagation. The SST effect on surface fluxes enhances variability ahead of the convection over both the Indian Ocean and the western Pacific, favoring northward propagation.

To quantitatively investigate the contribution of intraseasonal SST to the atmospheric BSISO convection, we compute budgets of $\langle m \rangle$ and $\partial \langle m \rangle / \partial t$. Column-integrated LW is the primary contributor to $\langle m \rangle$. $\langle m \rangle$ is destroyed by the vertical export over the Warm Pool region and horizonal advection over the equatorial oceans. In contrast, the horizonal advection of $\langle m \rangle$ is the most important driver of $\partial \langle m \rangle / \partial t$, with zonal advection contributing across almost the entire active BSISO region, accompanied by meridional advection contributing over the Bay of Bengal and South China Sea. During most of the BSISO life cycle, LH supports intraseasonal $\langle m \rangle$ but not $\partial \langle m \rangle / \partial t$, as the maximum LH slightly lags convection. It is interesting that SH supports not only the maintenance but also the generation of $\langle m \rangle$, though the amplitude is small. SST-modulated surface fluxes account for ~2% of $\langle m \rangle$ day^{-1} over the far western Indian Ocean, northern Arabian Sea, and Bay of Bengal, while they damp $\langle m \rangle$ over the western Pacific. This is associated with different phase relationships between convection and SST anomalies over these regions. Intraseasonal SST plays a more important role in $\partial \langle m \rangle / \partial t$, with a contribution of more than 12%. Intraseasonal SST variability enhances the propagation of BSISO convection across the active BSISO region.

In this study, the oceanic feedback to BSISO convection is diagnosed using the reanalysis through the SST influence on surface fluxes. SST fluctuations may affect the BSISO through other dynamic or thermal processes, such as boundary layer convergence induced by SST gradients. Previous modeling studies also found subdaily SST variability can influence the simulated BSISO (Hu et al., 2015; Klingaman et al., 2011) due to the intense SST diurnal cycle over the Asian summer monsoon region. Each of these processes may play an important role in the BSISO MSE budgets (especially $\partial \langle m \rangle / \partial t$), and each fundamentally relies on SH. Although SH variability is small compared to LH, it may play an important role in processes that contribute to BSISO propagation. It is necessary to consider LH and SH separately when assessing intraseasonal coupled feedbacks. These feedbacks should be examined using reanalysis data sets across the BSISO region and throughout the BSISO life cycle. Comprehensive understanding of ocean feedbacks to the BSISO using reanalysis is a key tool to investigate the ocean coupling in model simulations and then help improve the accuracy of BSISO simulations. Future work should apply these methods to assess the influence of ocean coupling on the BSISO in current model simulations.

Acknowledgments
Y. G. and P-C. H. are supported by the National Key R&D Program of China (2018YFC1505804) and China Scholarship Council (File No. 201708320302). N. P. K. is supported by an Independent Research Fellowship from the UK Natural Environment Research Council (NE/L010976/1). C. A. D. is supported by NSF award AGS-1445191. All data required to reproduce the figures in this paper can be obtained from the following DOIs: 10.6084/m9.figshare.6743450 and 10.6084/m9.figshare.6743429. The data files contained at these DOIs are the output from the air-sea diagnostic software package applied to the MERRA and ERA-Interim reanalyses, respectively.

References

Adames, Á. F., & Wallace, J. M. (2015). Three-dimensional structure and evolution of the moisture field in the MJO. *Journal of the Atmospheric Sciences*, *72*(10), 3733–3754. https://doi.org/10.1175/JAS-D-15-0003.1

Ajayamohan, R. S., Annamalai, H., Luo, J.-J., Hafner, J., & Yamagata, T. (2011). Poleward propagation of boreal summer intraseasonal oscillations in a coupled model: Role of internal processes. *Climate Dynamics*, *37*(5–6), 851–867. https://doi.org/10.1007/s00382-010-0839-6

Andersen, J. A., & Kuang, Z. (2012). Moist static energy budget of MJO-like disturbances in the atmosphere of a zonally symmetric aquaplanet. *Journal of Climate*, *25*(8), 2782–2804. https://doi.org/10.1175/JCLI-D-11-00168.1

Bellon, G., & Sobel, A. H. (2008). Instability of the axisymmetric monsoon flow and intraseasonal oscillation. *Journal of Geophysical Research*, *113*, D07108. https://doi.org/10.1029/2007JD009291

Bentamy, A., Piollé, J. F., Grouazel, A., Danielson, R., Gulev, S., Paul, F., Azelmat, H., et al. (2017). Review and assessment of latent and sensible heat flux accuracy over the global oceans. *Remote Sensing of Environment*, *201*, 196–218. https://doi.org/10.1016/j.rse.2017.08.016

Biello, J. A., & Majda, A. J. (2005). A new multiscale model for the Madden–Julian Oscillation. *Journal of the Atmospheric Sciences*, *62*(6), 1694–1721. https://doi.org/10.1175/JAS3455.1

Bladé, I., & Hartmann, D. L. (1993). Tropical intraseasonal oscillations in a simple nonlinear model. *Journal of the Atmospheric Sciences*, *50*(17), 2922–2939. https://doi.org/10.1175/1520-0469(1993)050<2922:TIOIAS>2.0.CO;2

Brunke, M. A., Wang, Z., Zeng, X., Bosilovich, M., & Shie, C.-L. (2011). An assessment of the uncertainties in ocean surface turbulent fluxes in 11 reanalysis, satellite-derived, and combined global datasets. *Journal of Climate*, *24*(21), 5469–5493. https://doi.org/10.1175/2011JCLI4223.1

Chen, T.-C., & Murakami, M. (1988). The 30–50 day variation of convective activity over the western Pacific Ocean with emphasis on the northwestern region. *Monthly Weather Review*, *116*(4), 892–906. https://doi.org/10.1175/1520-0493(1988)116<0892:TDVOCA>2.0.CO;2

Chou, C., & Hsueh, Y.-C. (2010). Mechanisms of northward-propagating intraseasonal oscillation—A comparison between the Indian Ocean and the western North Pacific. *Journal of Climate*, *23*(24), 6624–6640. https://doi.org/10.1175/2010JCLI3596.1

DeMott, C. A., Benedict, J. J., Klingaman, N. P., Woolnough, S. J., & Randall, D. A. (2016). Diagnosing ocean feedbacks to the MJO: SST-modulated surface fluxes and the moist static energy budget: Ocean feedbacks and the MJO. *Journal of Geophysical Research: Atmospheres*, *121*, 8350–8373. https://doi.org/10.1002/2016JD025098

DeMott, C. A., Klingaman, N. P., & Woolnough, S. J. (2015). Atmosphere-ocean coupled processes in the Madden-Julian oscillation: air-sea coupling and the MJO. *Reviews of Geophysics*, *53*, 1099–1154. https://doi.org/10.1002/2014RG000478

DeMott, C. A., Stan, C., & Randall, D. A. (2013). Northward propagation mechanisms of the boreal summer intraseasonal oscillation in the ERA-Interim and SP-CCSM. *Journal of Climate*, *26*(6), 1973–1992. https://doi.org/10.1175/JCLI-D-12-00191.1

DeMott, C. A., Stan, C., Randall, D. A., & Branson, M. D. (2014). Intraseasonal variability in coupled GCMs: The roles of ocean feedbacks and model physics. *Journal of Climate*, *27*(13), 4970–4995. https://doi.org/10.1175/JCLI-D-13-00760.1

Donlon, C. J., Martin, M., Stark, J., Roberts-Jones, J., Fiedler, E., & Wimmer, W. (2012). The Operational Sea Surface Temperature and Sea Ice Analysis (OSTIA) system. *Remote Sensing of Environment*, *116*, 140–158. https://doi.org/10.1016/j.rse.2010.10.017

Duvel, J. P., Roca, R., & Vialard, J. (2004). Ocean mixed layer temperature variations induced by intraseasonal convective perturbations over the Indian Ocean. *Journal of the Atmospheric Sciences*, *61*(9), 1004–1023. https://doi.org/10.1175/1520-0469(2004)061<1004:OMLTVI>2.0.CO;2

Duvel, J. P., & Vialard, J. (2007). Indo-Pacific sea surface temperature perturbations associated with intraseasonal oscillations of tropical convection. *Journal of Climate*, *20*(13), 3056–3082. https://doi.org/10.1175/JCLI4144.1

Fu, X., & Wang, B. (2004). Differences of boreal summer intraseasonal oscillations simulated in an atmosphere–ocean coupled model and an atmosphere-only model. *Journal of Climate*, *17*, 9.

Fu, X., Wang, B., Li, T., & McCreary, J. P. (2003). Coupling between northward-propagating, intraseasonal oscillations and sea surface temperature in the Indian Ocean. *Journal of the Atmospheric Sciences*, *60*(15), 1733–1753. https://doi.org/10.1175/1520-0469(2003)060<1733:CBNIOA>2.0.CO;2

Fu, X., Wang, B., Waliser, D. E., & Tao, L. (2007). Impact of atmosphere–ocean coupling on the predictability of monsoon intraseasonal oscillations. *Journal of the Atmospheric Sciences*, *64*(1), 157–174. https://doi.org/10.1175/JAS3830.1

Gadgil, S., & Srinivasan, J. (1990). Low frequency variation of tropical convergence zones. *Meteorology and Atmospheric Physics*, *44*(1–4), 119–132. https://doi.org/10.1007/BF01026814

Gao, Y., Hsu, P.-C., & Li, T. (2018). Effects of high-frequency activity on latent heat flux of MJO. *Climate Dynamics*. https://doi.org/10.1007/s00382-018-4208-1

Gill, A. E. (1980). Some simple solutions for heat-induced tropical circulation. *Quarterly Journal of the Royal Meteorological Society*, *106*(449), 447–462. https://doi.org/10.1002/qj.49710644905

Hartmann, D. L., & Maloney, E. D. (2001). The Madden–Julian Oscillation, barotropic dynamics, and North Pacific tropical cyclone formation. Part II: Stochastic barotropic modeling. *Journal of the Atmospheric Sciences*, *58*, 12.

Hartmann, D. L., & Michelsen, M. L. (1989). Intraseasonal periodicities in Indian rainfall. *Journal of the Atmospheric Sciences*, *46*(18), 2838–2862. https://doi.org/10.1175/1520-0469(1989)046<2838:IPIIR>2.0.CO;2

Hartmann, D. L., Michelsen, M. L., & Klein, S. A. (1992). Seasonal variations of tropical intraseasonal oscillations: A 20–25-day oscillation in the western Pacific. *Journal of the Atmospheric Sciences*, *49*(14), 1277–1289. https://doi.org/10.1175/1520-0469(1992)049<1277:SVOTIO>2.0.CO;2

Hendon, H. H., & Glick, J. (1997). Intraseasonal air–sea interaction in the tropical Indian and Pacific Oceans. *Journal of Climate*, *10*, 15.

Hsu, H.-H., & Weng, C.-H. (2001). Northwestward propagation of the intraseasonal oscillation in the western North Pacific during the boreal summer: Structure and mechanism. *Journal of Climate*, *14*(18), 3834–3850. https://doi.org/10.1175/1520-0442(2001)014<3834:NPOTIO>2.0.CO;2

Hsu, P., & Li, T. (2012). Role of the boundary layer moisture asymmetry in causing the eastward propagation of the Madden–Julian Oscillation. *Journal of Climate*, *25*(14), 4914–4931. https://doi.org/10.1175/JCLI-D-11-00310.1

Hsu, P.-C., Lee, J.-Y., Ha, K.-J., & Tsou, C.-H. (2017). Influences of boreal summer intraseasonal oscillation on heat waves in monsoon Asia. *Journal of Climate*, *30*(18), 7191–7211. https://doi.org/10.1175/JCLI-D-16-0505.1

Hu, W., Duan, A., & Wu, G. (2015). Impact of subdaily air–sea interaction on simulating intraseasonal oscillations over the tropical Asian monsoon region. *Journal of Climate*, *28*(3), 1057–1073. https://doi.org/10.1175/JCLI-D-14-00407.1

Jiang, X., Li, T., & Wang, B. (2004). Structures and mechanisms of the northward propagating boreal summer Intraseasonal oscillation. *Journal of Climate*, *17*(5), 1022–1039. https://doi.org/10.1175/1520-0442(2004)017<1022:SAMOTN>2.0.CO;2

Johnson, R. H., Rickenbach, T. M., Rutledge, S. A., Ciesielski, P. E., & Schubert, W. H. (1999). Trimodal characteristics of tropical convection. *Journal of Climate*, *12*, 22.

Kawamura, R., Murakami, T., & Wang, B. (1996). Tropical and mid-latitude 45-day perturbations over the western Pacific during the northern summer. *Journal of the Meteorological Society of Japan. Ser. II*, *74*(6), 867–890. https://doi.org/10.2151/jmsj1965.74.6_867

Kemball-Cook, S., & Wang, B. (2001). Equatorial waves and air–sea interaction in the boreal summer intraseasonal oscillation. *Journal of Climate*, *14*, 20.

Kemball-Cook, S., Wang, B., & Fu, X. (2002). Simulation of the intraseasonal oscillation in the ECHAM-4 model: The impact of coupling with an ocean model. *Journal of the Atmospheric Sciences*, *59*(9), 1433–1453. https://doi.org/10.1175/1520-0469(2002)059<1433:SOTIOI>2.0.CO;2

Kemball-Cook, S. R., & Weare, B. C. (2001). The onset of convection in the Madden–Julian Oscillation. *Journal of Climate*, *14*(5), 780–793. https://doi.org/10.1175/1520-0442(2001)014<0780:TOOCIT>2.0.CO;2

Kiladis, G. N., Straub, K. H., & Haertel, P. T. (2005). Zonal and vertical structure of the Madden–Julian Oscillation. *Journal of the Atmospheric Sciences*, *62*(8), 2790–2809. https://doi.org/10.1175/JAS3520.1

Kiranmayi, L., & Maloney, E. D. (2011). Intraseasonal moist static energy budget in reanalysis data: Intraseasonal MSE budget in NCEP and ERA. *Journal of Geophysical Research*, *116*, D21117. https://doi.org/10.1029/2011JD016031

Klingaman, N. P., Inness, P. M., Weller, H., & Slingo, J. M. (2008). The importance of high-frequency sea surface temperature variability to the intraseasonal oscillation of Indian monsoon rainfall. *Journal of Climate*, *21*(23), 6119–6140. https://doi.org/10.1175/2008JCLI2329.1

Klingaman, N. P., Woolnough, S. J., Weller, H., & Slingo, J. M. (2011). The impact of finer-resolution air–sea coupling on the intraseasonal oscillation of the Indian monsoon. *Journal of Climate*, *24*(10), 2451–2468. https://doi.org/10.1175/2010JCLI3868.1

Krishnamurti, T. N., Oosterhof, D. K., & Mehta, A. V. (1988). Air–sea interaction on the time scale of 30 to 50 days. *Journal of the Atmospheric Sciences*, *45*(8), 1304–1322. https://doi.org/10.1175/1520-0469(1988)045<1304:AIOTTS>2.0.CO;2

Krishnamurti, T. N., & Subrahmanyam, D. (1982). The 30–50 day mode at 850 mb during MONEX. *Journal of the Atmospheric Sciences*, *39*(9), 2088–2095. https://doi.org/10.1175/1520-0469(1982)039<2088:TDMAMD>2.0.CO;2

Lau, K.-M., & Chan, P. H. (1986). Aspects of the 40–50 day oscillation during the northern summer as inferred from outgoing longwave radiation. *Monthly Weather Review*, *114*(7), 1354–1367. https://doi.org/10.1175/1520-0493(1986)114<1354:AOTDOD>2.0.CO;2

Lawrence, D. M., & Webster, P. J. (2002). The boreal summer intraseasonal oscillation: Relationship between northward and eastward movement of convection. *Journal of the Atmospheric Sciences*, *59*, 14.

Li, J., Mao, J., & Wu, G. (2015). A case study of the impact of boreal summer intraseasonal oscillations on Yangtze rainfall. *Climate Dynamics*, *44*(9–10), 2683–2702. https://doi.org/10.1007/s00382-014-2425-9

Lin, A., Li, T., Fu, X., Luo, J.-J., & Masumoto, Y. (2011). Effects of air–sea coupling on the boreal summer intraseasonal oscillations over the tropical Indian Ocean. *Climate Dynamics*, *37*(11–12), 2303–2322. https://doi.org/10.1007/s00382-010-0943-7

Lindzen, R. S., & Nigam, S. (1987). On the role of sea surface temperature gradients in forcing low-level winds and convergence in the tropics. *Journal of the Atmospheric Sciences*, *44*(17), 2418–2436. https://doi.org/10.1175/1520-0469(1987)044<2418:OTROSS>2.0.CO;2

Madden, R. A. (1986). Seasonal variations of the 40-50 day oscillation in the tropics. *Journal of the Atmospheric Sciences*, *43*(24), 3138–3158. https://doi.org/10.1175/1520-0469(1986)043<3138:SVOTDO>2.0.CO;2

Madden, R. A., & Julian, P. R. (1971). Detection of a 40–50 day oscillation in the zonal wind in the tropical Pacific. *Journal of the Atmospheric Sciences*, *28*(5), 702–708. https://doi.org/10.1175/1520-0469(1971)028<0702:DOADOI>2.0.CO;2

Madden, R. A., & Julian, P. R. (1972). Description of global-scale circulation cells in the tropics with a 40–50 day period. *Journal of the Atmospheric Sciences*, *29*(6), 1109–1123. https://doi.org/10.1175/1520-0469(1972)029<1109:DOGSCC>2.0.CO;2

Maloney, E. D. (2009). The moist static energy budget of a composite tropical intraseasonal oscillation in a climate model. *Journal of Climate*, *22*(3), 711–729. https://doi.org/10.1175/2008JCLI2542.1

Mapes, B. E., & Bacmeister, J. T. (2012). Diagnosis of tropical biases and the MJO from patterns in the MERRA analysis tendency fields. *Journal of Climate*, *25*(18), 6202–6214. https://doi.org/10.1175/JCLI-D-11-00424.1

Murakami, T. (1980). Empirical orthogonal function analysis of satellite-observed outgoing longwave radiation during summer. *Monthly Weather Review*, *108*(2), 205–222. https://doi.org/10.1175/1520-0493(1980)108<0205:EOFAOS>2.0.CO;2

Murakami, T., & Nakazawa, T. (1985). Tropical 45 day oscillations during the 1979 Northern Hemisphere summer. *Journal of the Atmospheric Sciences*, *42*(11), 1107–1122. https://doi.org/10.1175/1520-0469(1985)042<1107:TDODTN>2.0.CO;2

Neelin, J. D., & Held, I. M. (1987). Modeling tropical convergence based on the moist static energy budget. *Monthly Weather Review*, *115*(1), 3–12. https://doi.org/10.1175/1520-0493(1987)115<0003:MTCBOT>2.0.CO;2

Neena, J. M., Waliser, D., & Jiang, X. (2017). Model performance metrics and process diagnostics for boreal summer intraseasonal variability. *Climate Dynamics*, *48*(5–6), 1661–1683. https://doi.org/10.1007/s00382-016-3166-8

Peters, O., & Neelin, J. D. (2006). Critical phenomena in atmospheric precipitation. *Nature Physics*, *2*(6), 393–396. https://doi.org/10.1038/nphys314

Praveen Kumar, B., Vialard, J., Lengaigne, M., Murty, V. S. N., & McPhaden, M. J. (2012). TropFlux: Air-sea fluxes for the global tropical oceans—Description and evaluation. *Climate Dynamics*, *38*(7–8), 1521–1543. https://doi.org/10.1007/s00382-011-1115-0

Rajendran, K., & Kitoh, A. (2006). Modulation of tropical intraseasonal oscillations by ocean–atmosphere coupling. *Journal of Climate*, *19*(3), 366–391. https://doi.org/10.1175/JCLI3638.1

Raymond, D. J. (2000). Thermodynamic control of tropical rainfall. *Quarterly Journal of the Royal Meteorological Society*, *126*(564), 889–898. https://doi.org/10.1002/qj.49712656406

Ren, X., Yang, X.-Q., & Sun, X. (2013). Zonal oscillation of western Pacific subtropical high and subseasonal SST variations during Yangtze persistent heavy rainfall events. *Journal of Climate*, *26*(22), 8929–8946. https://doi.org/10.1175/JCLI-D-12-00861.1

Reynolds, R. W., Rayner, N. A., & Smith, T. M. (2002). An improved in situ and satellite SST analysis for climate. *Journal of Climate*, *15*, 17.

Rienecker, M. M., Suarez, M. J., Gelaro, R., Todling, R., Bacmeister, J., Liu, E., et al. (2011). MERRA: NASA's Modern-Era Retrospective Analysis for Research and Applications. *Journal of Climate*, *24*(14), 3624–3648. https://doi.org/10.1175/JCLI-D-11-00015.1

Roxy, M., & Tanimoto, Y. (2012). Influence of sea surface temperature on the intraseasonal variability of the South China Sea summer monsoon. *Climate Dynamics*, *39*(5), 1209–1218. https://doi.org/10.1007/s00382-011-1118-x

Roxy, M., Tanimoto, Y., Preethi, B., Terray, P., & Krishnan, R. (2013). Intraseasonal SST-precipitation relationship and its spatial variability over the tropical summer monsoon region. *Climate Dynamics*, *41*(1), 45–61. https://doi.org/10.1007/s00382-012-1547-1

Sanchez-Franks, A., Kent, E. C., Matthews, A. J., Webber, B. G. M., Peatman, S. C., & Vinayachandran, P. N. (2018). Intraseasonal variability of air-dea fluxes over the Bay of Bengal during the southwest monsoon. *Journal of Climate*, *31*(17), 7087–7109. https://doi.org/10.1175/JCLI-D-17-0652.1

Seo, K.-H., Schemm, J.-K. E., Wang, W., & Kumar, A. (2007). The boreal summer intraseasonal oscillation simulated in the NCEP Climate Forecast System: The effect of sea surface temperature. *Monthly Weather Review*, *135*(5), 1807–1827. https://doi.org/10.1175/MWR3369.1

Sobel, A., Wang, S., & Kim, D. (2014). Moist static energy budget of the MJO during DYNAMO. *Journal of the Atmospheric Sciences*, *71*(11), 4276–4291. https://doi.org/10.1175/JAS-D-14-0052.1

Straub, K. H., & Kiladis, G. N. (2003). Interactions between the boreal summer intraseasonal oscillation and higher-frequency tropical wave activity. *Monthly Weather Review*, *131*, 16.

Sun, X., Jiang, G., Ren, X., & Yang, X.-Q. (2016). Role of intraseasonal oscillation in the persistent extreme precipitation over the Yangtze River Basin during June 1998: Intraseasonal oscillations in 1998 PEPE. *Journal of Geophysical Research: Atmospheres*, *121*, 10,453–10,469. https://doi.org/10.1002/2016JD025077

Waliser, D. E., & Graham, N. E. (1993). Convective cloud systems and warm-pool sea surface temperatures: Coupled interactions and self-regulation. *Journal of Geophysical Research*, *98*, 12,881–12,893. https://doi.org/10.1029/93JD00872

Wang, B., & Liu, F. (2011). A model for scale interaction in the Madden–Julian Oscillation. *Journal of the Atmospheric Sciences*, *68*(11), 2524–2536. https://doi.org/10.1175/2011JAS3660.1

Wang, B., & Rui, H. (1990). Dynamics of the coupled moist Kelvin–Rossby wave on an equatorial β-plane. *Journal of the Atmospheric Sciences*, *47*(4), 397–413. https://doi.org/10.1175/1520-0469(1990)047<0397:DOTCMK>2.0.CO;2

Wang, B., & Xie, X. (1996). Low-frequency equatorial waves in vertically sheared zonal flow. Part I: Stable waves. *Journal of the Atmospheric Sciences*, *53*(3), 449–467. https://doi.org/10.1175/1520-0469(1996)053<0449:LFEWIV>2.0.CO;2

Wang, B., & Xie, X. (1997). A model for the boreal summer intraseasonal oscillation. *Journal of the Atmospheric Sciences*, *54*(1), 72–86. https://doi.org/10.1175/1520-0469(1997)054<0072:AMFTBS>2.0.CO;2

Wang, T., Yang, X.-Q., Fang, J., Sun, X., & Ren, X. (2018). Role of air–sea interaction in the 30–60-day boreal summer intraseasonal oscillation over the western North Pacific. *Journal of Climate*, *31*(4), 1653–1680. https://doi.org/10.1175/JCLI-D-17-0109.1

Weare, B. C., Strub, P. T., & Samuel, M. D. (1981). Annual mean surface heat fluxes in the tropical Pacific Ocean. *Journal of Physical Oceanography*, *11*(5), 705–717.

Webster, P. J., Magaña, V. O., Palmer, T. N., Shukla, J., Tomas, R. A., Yanai, M., & Yasunari, T. (1998). Monsoons: Processes, predictability, and the prospects for prediction. *Journal of Geophysical Research*, *103*, 14,451–14,510. https://doi.org/10.1029/97JC02719

Webster, P. J. (1983). Mechanisms of monsoon low-frequency variability: Surface hydrological effects. *Journal of the Atmospheric Sciences*, *40*(9), 2110–2124. https://doi.org/10.1175/1520-0469(1983)040<2110:MOMLFV>2.0.CO;2

Woolnough, S. J., Slingo, J. M., & Hoskins, B. J. (2000). The relationship between convection and sea surface temperature on intraseasonal timescales. *Journal of Climate*, *13*(12), 2086–2104. https://doi.org/10.1175/1520-0442(2000)013<2086:TRBCAS>2.0.CO;2

Woolnough, S. J., Vitart, F., & Balmaseda, M. A. (2007). The role of the ocean in the Madden–Julian Oscillation: Implications for MJO prediction. *Quarterly Journal of the Royal Meteorological Society*, *133*(622), 117–128. https://doi.org/10.1002/qj.4

Wu, R., & Wang, B. (2001). Multi-stage onset of the summer monsoon over the western North Pacific. *Climate Dynamics*, *17*(4), 277–289. https://doi.org/10.1007/s003820000118

Xie, X., & Wang, B. (1996). Low-frequency equatorial waves in vertically sheared zonal flow. Part II: Unstable waves. *Journal of the Atmospheric Sciences*, *53*(23), 3589–3605. https://doi.org/10.1175/1520-0469(1996)053<3589:LFEWIV>2.0.CO;2

Yasunari, T. (1979). Cloudiness fluctuations associated with the northern summer monsoon. *Journal of the Meteorological Society of Japan*, *57*(3), 16.

Zhou, C., & Li, T. (2010). Upscale feedback of tropical synoptic variability to intraseasonal oscillations through the nonlinear rectification of the surface latent heat flux. *Journal of Climate*, *23*(21), 5738–5754. https://doi.org/10.1175/2010JCLI3468.1

Zhou, W., & Chan, J. C. L. (2005). Intraseasonal oscillations and the South China Sea summer monsoon onset. *International Journal of Climatology*, *25*(12), 1585–1609. https://doi.org/10.1002/joc.1209